AGRICULTURAL UNIVERSITY – PLOVDIV

FACULTY OF AGRONOMY

DEPARTMENT OF CROP SCIENCE

IVELIN DIMITROV MARKOV

INVESTIGATE THE IMPACT OF DIFFERENT SUSTAINABLE TURF MANAGEMENT PRACTICES ON SOIL C SEQUESTRATION ON INTENSIVELY MAINTAINED SAND-BASED PUTTING GREENS AND HOW THEIR IMPLEMENTATION AFFECTS THE ANNUAL CARBON BUDGET

AUTHOR'S ABSTRACT

of a dissertation for the award of the educational and scientific degree

"DOCTOR"

In "Forage Production and Grassland Management"

SCIENTIFIC SUPERVISORS:

Assoc. Prof. Dr. Atanas Sevov

PLOVDIV

2026

The studies were conducted during the period 2019–2025 at two golf courses in Bulgaria and China.

The dissertation comprises 243 pages and includes 43 tables and 94 figures. The cited literature includes 456 sources in Latin script.

The dissertation was discussed at an extended departmental council meeting of the Department of “Crop Science” at the Faculty of Agronomy, Agricultural University – Plovdiv.

The dissertation defence will take place on ___ . ___ . 2026 at ___ hours in the meeting hall of AU – Plovdiv, before a Specialized Scientific Jury approved by Rector’s Order RD of ___ . ___ . 2026.

Reviews from:

Statements from:

The defence materials are available to interested parties in the library of the Agricultural University – Plovdiv.

Please send reviews and comments to:

Ivomarkov2003@yahoo.com

1 Introduction

Turfgrass systems occupy a substantial share of the global land surface, with grasslands covering approximately 31 to 43% of total land area. Alongside natural grasslands, a rapidly expanding share of this coverage is now represented by managed turf in urban and semi-urban environments. Increasing urbanization replaces forests and agricultural lands with maintained green areas such as lawns, meadows, parks, sports fields, and golf courses. In the United States, intensively maintained urban grassland systems are estimated to occupy about 163,800 km², approximately 2% of the continental U.S. land area, and an area roughly three times larger than that used for irrigated corn.

Within this green infrastructure, sports turf and golf courses represent a high-profile and management-intensive component. The U.S. alone includes approximately 700,000 sports fields and 16,750 golf courses, within a global total of 38,886 courses. Importantly, 78% of the world's golf courses are concentrated in only 10 countries, which highlights both the geographic concentration and the potential environmental footprint of intensively managed turf systems.

Golf courses, and putting greens in particular, exemplify the tension between performance requirements and environmental responsibility. Players expect smooth, fast, visually uniform putting surfaces. Meeting these expectations typically requires intensive practices such as frequent mowing at very low cutting heights, targeted fertilization, and precisely scheduled irrigation. These operations can be resource-demanding, increasing consumption of water, energy, and nutrients, while also elevating the risk of undesirable outcomes such as nutrient leaching when inputs are not aligned with plant demand and soil retention capacity.

At the same time, golf course managers face growing pressure from regulatory frameworks and public expectations to reduce chemical inputs, conserve water, and demonstrate stewardship. This dual requirement, elite playing quality plus sustainability, creates a strong need for approaches that are both physiologically grounded and operationally practical, allowing decisions to adapt to changing weather and stress conditions rather than relying on static schedules.

Soils are a central component of the global carbon cycle, storing more carbon than the atmosphere and terrestrial vegetation combined. Managed turfgrass systems may contribute to carbon sequestration through root biomass production and accumulation of organic matter at the surface and within the rootzone. However, the net climate benefit of turf systems depends on how management affects both carbon inputs (biomass, organic matter accumulation) and carbon costs (energy use, fertilizer-related emissions, and accelerated nutrient cycling).

Golf courses are heterogeneous systems in which highly managed greens and tees typically account for only about 5% of maintained turf area, while fairways and roughs represent roughly 25 to 35% and 60%, respectively. Larger, lower-input areas may act as carbon sinks under conservative management, whereas intensive inputs and frequent mechanical

operations can increase greenhouse gas emissions and offset carbon gains. Therefore, the core challenge is not simply whether turf can store carbon, but how management can shift the annual carbon budget toward net sequestration without compromising the functional performance of the playing surface.

Rising concern over climate change, water scarcity, and nutrient runoff has increased the demand for Precision Turfgrass Management (PTM). While precision tools are common in agriculture, their uptake in turf remains comparatively limited. Integrating real-time soil and weather sensing, vegetation indices (VIs) from UAV or satellite imagery, and AI-driven analytics creates an opportunity to improve irrigation and fertilization efficiency, reduce nutrient losses, and detect turf stress earlier and more spatially precisely than visual scouting alone. These capabilities support a shift from reactive management to predictive, evidence-based scheduling.

Modern high-performance golf greens are commonly constructed to USGA or California specifications, using sand-based rootzones (typically at least 90% sand) with optional amendments to improve water and nutrient retention. Sand-based profiles provide rapid drainage, firm playing surfaces, and reduced compaction risk, which is essential under constant traffic and mechanical stress.

These performance advantages also create intrinsic management constraints. Sand has low cation exchange capacity and limited water-holding capacity; therefore, nutrient and water inputs can be rapidly leached or depleted unless applied with precision. Moisture deficits can develop quickly during heat or drought. As a result, sand-based greens require careful scheduling and dosage of irrigation and fertilization to prevent both drought stress and excessive leaching.

To achieve consistent ball roll and aesthetics, greens are usually mowed daily (and sometimes twice daily in tournament conditions) at cutting heights as low as 1.8 to 3 mm. Such close mowing reduces leaf area, constrains photosynthesis, and can limit root development, while repeated mechanical wear contributes to micro-compaction. These stresses often lead to increased reliance on inputs, which must be carefully managed to avoid conflicts with sustainability objectives.

Nitrogen fertilization is a key driver of turf performance but also a frequent source of inefficiency when misaligned with demand. Excess nitrogen can increase shoot growth, thatch accumulation, and disease pressure, while insufficient nitrogen reduces color, density, and recovery capacity. In sand-based systems, where nutrient retention is limited, the margin for error is narrow. Irrigation management is similarly critical: maintaining suitable volumetric water content (VWC) requires avoiding both drought stress and overwatering, with precision irrigation increasingly supported by soil moisture sensors and evapotranspiration (ET) estimates. Greens are also subjected to aeration, verticutting, topdressing, and occasional scarification to manage compaction and thatch. These interventions are necessary but resource-intensive and can temporarily disrupt play, which further emphasizes the value of optimising timing and intensity.

Sand-based putting greens present a management paradox. Perennial turf may sequester carbon through roots and organic matter accumulation. At the same time, high-intensity inputs and frequent operations can increase energy use and emissions and accelerate nutrient turnover, potentially reducing net carbon benefits. Moreover, excessive organic matter accumulation can compromise playing characteristics and rootzone function, even if it increases carbon storage. The scientific and practical aim is therefore to define maintenance routines that sustain elite turf quality while improving the net soil carbon balance and reducing unnecessary resource use.

2 Materials and methods

This dissertation is organised into five interrelated parts that collectively address sustainable management of intensively maintained sand-based putting greens and provide the inputs for an integrated SMART Decision Support System (DSS).

Part 1: Optimising nitrogen fertilisation. Nitrogen demand is modelled using temperature-based growth potential (GP), lagged vegetation indices, and stress-aligned environmental variables to support adaptive scheduling at daily to weekly timescales, with outputs suitable for operational integration into a DSS.

Part 2: Irrigation optimisation. Fixed-schedule irrigation is compared with ET-based approaches, focusing on distribution uniformity (DU), VWC, turf response, and water-use efficiency (WUE). Results define thresholds and scheduling parameters for integration into the DSS.

Part 3: Root system development. Root growth patterns are quantified and related to environmental and management factors, including contrasting irrigation strategies. The objective is to identify parameters that can inform predictive root-growth modelling and link mechanistically to fertilisation and irrigation decisions.

Part 4: Vegetation indices and remote sensing. Multiple VIs are evaluated for sensitivity to irrigation, fertilisation, and root development, and related to in-situ measurements (soil moisture, clipping volume, fertilisation). Computer vision UNet model is specifically developed and trained to classify golf course features and provide spatially detailed management cues for the DSS.

Part 5: AI-based Bayesian Decision Support System (BN-DSS). Outputs from Parts 1 to 4 are integrated into a modular Bayesian DSS, supported by machine learning and explainable AI (SHAP), to deliver site-specific recommendations that balance turf performance, resource conservation, and soil carbon sequestration goals.

The methodological workflow is summarized schematically in **Figure 3 (Methodological workflow)**, which links the primary objective (soil carbon sequestration and annual carbon budget on intensively managed sand-based putting greens) to four secondary objectives (optimizing N fertilization, optimizing irrigation rate, tracking root development, and remote

sensing/VIs) and to the final outcome: an AI-based SMART decision support system (DSS) built on a Bayesian Network (BN) foundation.

The study applies an **observational (non-replicated) design**, rather than a controlled, replicated field experiment. Each location represents a distinct agroecological and management context that mirrors real-world decision-making constraints in golf course maintenance. This design limits strict cause-and-effect attribution, but captures realistic heterogeneity and improves transferability of findings to operational turf management. Comparisons between sites are used to distinguish broadly effective strategies from those requiring local adjustment. Greens and sampling areas were selected to represent variation in soil characteristics, topography (high, medium, low elevation positions), and management histories.

Golf Course A (GCA) - is located at **43.41°N, 28.22°E**, ~1 km from the Black Sea, at **175 m altitude**, with a moderate-continental climate influenced by maritime proximity (mean annual T ~12°C; summer highs ~32°C; winter lows ~-2°C; annual precipitation ~550 mm, concentrated in spring/autumn, with common summer droughts). Prevailing north-northeast winds in late summer increase ET and contribute to moisture stress. The 2023–2024 growing seasons (1.03–30.10) were dry (335 mm and 480 mm precipitation), with warmer July–August conditions and elevated seasonal ET (910 mm and 955 mm).

Greens are built to **USGA specifications** (approximately **95% sand and 5% zeolite**). Following ~12 years of suboptimal maintenance, surface OM accumulated to **6–8% in the top 5 cm**, reducing infiltration and gas exchange, promoting shallow rooting, and increasing hydrophobicity risk. Agrostis Stolonifera is the used cultivar – 16 years old.

Historically, irrigation scheduling was not tightly linked to measured soil moisture ("deep and infrequent" approach), seasonal N-P-K applications did not fully match plant physiological demand, and cultural practices were insufficient to mitigate thatch accumulation. Growing-season mowing height is 3.0–3.2 mm; rolling is infrequent and event-driven.

Golf Course B (GCB) is located at **39.16°N, 116.99°E**, ~10 m above sea level and ~70 km inland from the Bohai Sea, with a humid continental climate and strong monsoonal influence (hot humid summers up to 35°C; annual precipitation ~590 mm; July–August totals of ~600 mm in both 2023 and 2024; cold dry winters to -12°C).

Greens are also USGA-based, with a rootzone of **94% sand, 4% silt, 2% clay**; pH 6.3–6.8; OM maintained near **~2.0%**, supporting high infiltration and stable water-holding capacity. Management is highly structured: VWC monitoring (target 18–22%), data-driven fertilization aligned with soil/tissue testing, monthly aeration/verticutting/light sand topdressing (intensified during monsoon periods), mowing at 3 mm, and rolling every alternate day. Agrostis Stolonifera is the used cultivar – 16 years old.

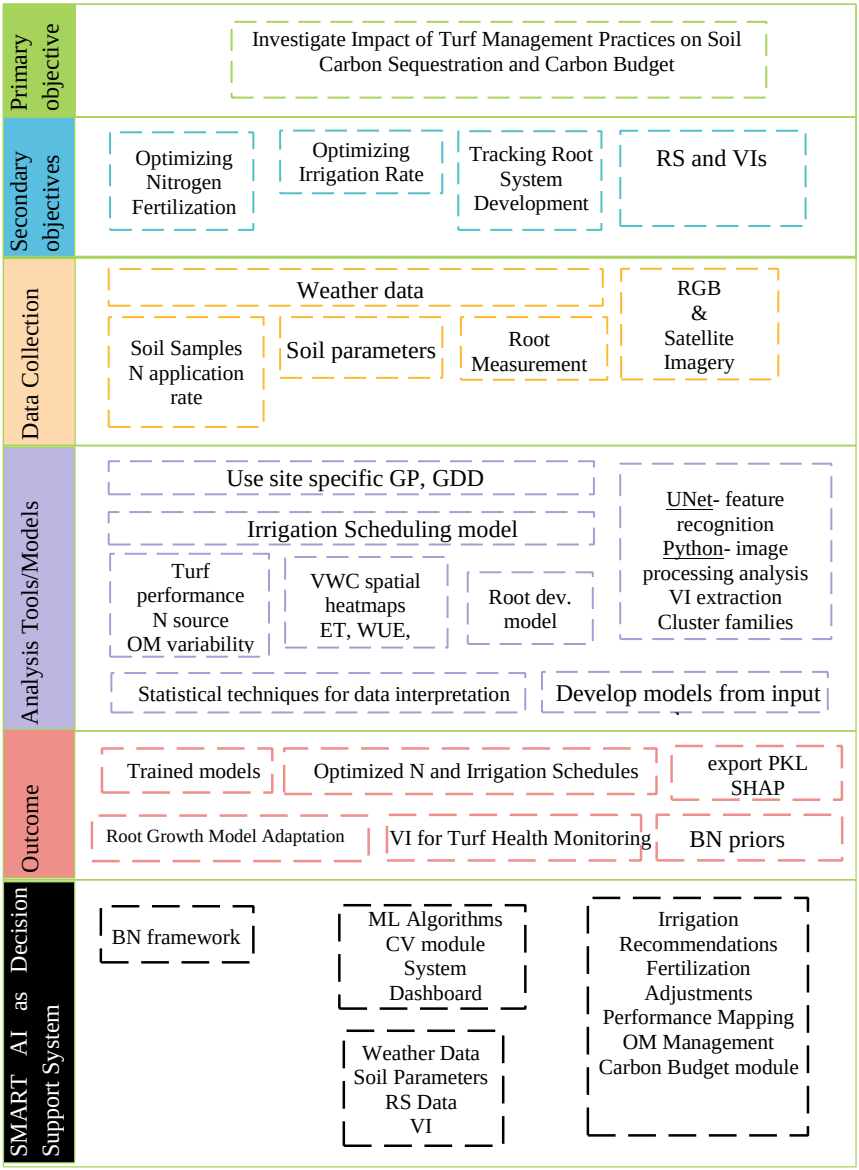

Figure 1. Methodological workflow

Weather and ET data - Automated weather stations at each course recorded **air temperature, relative humidity, solar radiation, wind speed, and precipitation** at **15-min intervals**, producing aggregated hourly and daily summaries. These data supported: (i) **Growth**

Potential (GP) calculated from air temperature for cool-season turf metabolic activity and N requirement modelling; (ii) **ET_0** estimated using the **Penman–Monteith** equation; and (iii) **Kc** values derived from cool-season turf literature and adjusted seasonally, with **$ETc = ET_0 \times Kc$** used for irrigation analyses. Weather and ET outputs were merged daily with clipping, soil moisture, VI, and management logs into time-aligned datasets used across models.

Soil and rootzone measurements - Soil cores were collected at both locations at **0–25 mm, 25–50 mm, and 50–75 mm** depths using a standard corer. Samples were analyzed for **pH, total N, P, K, OM distribution with depth, and total carbon**, following standard protocols (Kjeldahl for N; Mehlich-3 for P and K). Sampling targeted peak growth and transitional periods (spring green-up; autumn slowdown) to capture seasonal nutrient dynamics and support soil C stock estimates and associations with management practices.

Volumetric water content (VWC) - Handheld **TDR** sensors measured VWC at a standardized depth (**150 mm**), with periodic cross-checks against automated probes. At **GCA**, VWC was measured at fixed points weekly (more frequently during stress periods). At **GCB**, a TDR grid captured spatial patterns at least weekly; VWC maps were generated via ordinary kriging, enabling analysis of irrigation uniformity and moisture–stress interactions.

Turf and root measurements - **Clipping volume** was measured at GCA after each mowing event (graduated containers) as a proxy for growth/productivity. Data were collected from greens receiving GP, +25% GP, and -25% GP N rates, split by irrigation regimes (D and WD AOIs). **Thatch thickness** was measured periodically. Plugs were collected, **1 kg weight is** applied; **compressed thatch depth (mm)** was recorded to reduce variability. **Root measurements** were derived from soil cores collected at fixed sampling points; cores were washed and **root length** measured weekly (1.04–16.09 in 2023; 6.04–28.09 in 2024). Pin positions were rotated to capture spatial variability without repeatedly sampling the same spot. Sampling locations were selected away from edges and high-traffic zones (flat central areas, ≥1.5 m from perimeter). A standard golf hole cutter (112 mm diameter) extracted cores to **240 mm depth**; samples were labelled by date and green ID.

Part 1: Optimizing nitrogen fertilization

Nitrogen strategies were guided by GP. At **GCA**, a base **100% GP** rate was **3.5 g N m^{-2} $month^{-1}$** (0.9 g N m^{-2} $week^{-1}$), with **+25% GP** (1.125 g N m^{-2} $week^{-1}$) and **−25% GP** (0.675 g N m^{-2} $week^{-1}$) treatments. Weekly adjustments were made in response to climatic conditions. The GCA study period is reported as **01 March 2021 to 31 October 2023**, while other maintenance practices were kept consistent. At **GCB**, a similar GP-based framework was adopted with **100% GP = 40 g N m^{-2} $month^{-1}$** (1 g N m^{-2} $week^{-1}$), adjusted weekly to match regional climatic conditions.

Granular applications were delivered with a calibrated walk-behind spreader; foliar sprays (with surfactants) were used during peak demand or recovery phases using a calibrated boom sprayer with defined nozzle output and ground speed. Nitrogen modelling used merged daily datasets including fertilization records (N and cumulative acc_N_rate), VIs, environmental

variables (e.g., Tmax, Tmin, ET, precipitation, RH, wind, GP, PAR), and derived stress indicators. AOI-level fertilization labels were retained for crosschecks but N prediction was performed at whole-green temporal resolution. SHAP analysis was applied to HistGradientBoosting models fitted on aligned predictor sets to interpret feature contributions.

Part 2: Predicting soil moisture and optimizing irrigation rate

Irrigation optimisation integrated VWC measurements, ET estimation, and (at GCB) spatial VWC mapping. Irrigation system performance was assessed using **Distribution Uniformity (DU)** and **Coefficient of Variation (CV)**, with DU derived from catch-can audits (lowest quarter average divided by overall average). Water productivity metrics included **WUE** (clipping yield/total water input), **IWUE** (clipping yield/irrigation volume), and **HUE** (clipping yield/accumulated heat units, GDD).

At **GCA**, irrigation followed a preset schedule of ~35 mm/week including rainfall (D), while a deficit irrigation (WD) approach replenished ~80% of field capacity using ET estimates and in situ VWC. The sprinkler system delivered **5.2 mm m⁻² per 10 min** with DU ~72%. At **GCB**, irrigation was ET-based with ~80% replenishment, VWC monitoring at 15 cm depth, and delivery **6.8 mm m⁻² per 10 min** with DU ~81% (AOI DU values reported for S_3, S_4, W_9). GCB spatial mapping used a 5 m TDR grid and kriging; AOI perimeters and grids were managed via KML/JSON structures and visualised as heatmaps with computed CV. A soil water balance (SWB) approach and FAO-56 single Kc framework were used to compute depletion and ET components, with stress categories illustrated schematically (Figure 20).

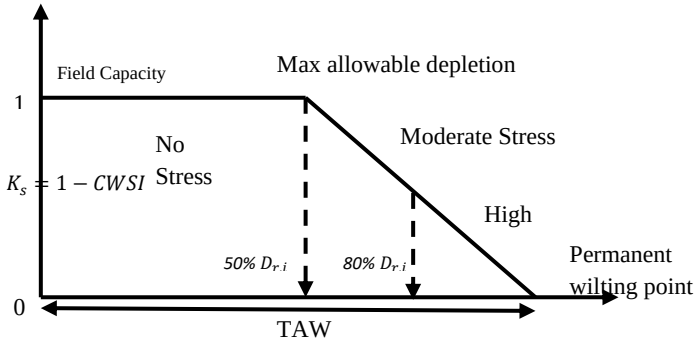

Figure 2. Schematic representation of water stress in the rootzone

Part 3: Tracking root system development

Root development was quantified using the weekly core-based root measurements and aligned with VWC, thatch/OM indicators, fertilization rates (GP, ±25%), and irrigation regimes (D, WD). Analyses included correlation and regression testing of moisture availability, OM management practices (aeration/topdressing), and fertilization regime

effects on root depth and length metrics, alongside temporal comparisons (seasonal patterns). Multivariate exploratory analyses (PCA/PLS) were used to identify which variables most strongly explained variation in root development, and outputs were prepared as decision-support inputs for the AI framework.

Part 4: Remote sensing and vegetative indices (VIs)

Ground-based RGB images were captured weekly at ~1.5 m height using fixed camera settings, aligned to soil/root sampling locations. UAV imagery (FIMI S2) was collected using standardised flight altitude and overlap (70% forward, 60% side), under clear midday conditions, with georeferencing via GCPs or GPS. Multispectral satellite data were acquired from PlanetScope (8 bands: Coastal Blue to NIR; Table 14), with imagery selected as cloud-free and collected over multi-year seasonal windows (Table 15). Image preprocessing included orthorectification, visual processing (sun angle correction, sharpening, color curve), and surface reflectance processing. A UNet model trained on annotated UAV imagery produced pixel-level AOI masks for greens/fairways; VIs were computed within masks only. A suite of indices (Table 17) was extracted, integrated with soil/root/environmental datasets, and analysed through time-series, regression, and ML approaches. A multi-season clustering workflow (mean, variance, trend per pixel; k-means k=10) generated canopy regime maps and supported VI-family similarity grouping via hierarchical clustering (Ward linkage).

Table 1. PlanetScope multispectral images bands

Band Nr.		**Wave length**
1	Coastal Blue	431 - 452 nm
2	Blue	465 - 515 nm
3	Green I	513 - 549 nm
4	Green II	547 - 583 nm
5	Yellow	600 - 620 nm
6	Red	650 - 680 nm
7	Red-Edge	697 - 713 nm
8	NIR	845 - 885 nm
-	RGB	-

Table 2. GCA and GCB satellite image collection

GCA			GCB	
Images	**Season**	**Year**	**Season**	**Images**
43	14.06-01.10	2019		
66	06.04-26.11	2020		
94	04.03-25.11	2021	21.03-01.12	52
94	15.03-26.11	2022	1.03-30.11	100
92	08.03-30.11	2023	1.03-30.11	64
103	05.03-28.11	2024	1.03-29.11	77
88	05.03-24.11	2025	4.03-25.11	94

Table 3. Collection of extracted VIs from satellite imagery

NDVI	MGVRI	GLI	MPRI	EXG	VARI	GNDVI	IRPVI	GRNDVI
GBNDVI	SAVI	MSAVI	GOSAVI	RVI	IPVI	DVI	MSR	NLI

Part 5: AI-based SMART/DS framework development

The DSS follows a four-step process integrating literature-derived knowledge with site-specific data. Step 1 extracts causal priors from literature via NLP pipelines; Step 2 encodes these priors into an initial BN with discretised node states (examples provided for NDVI, irrigation rate, N-rate states) and evaluates BN predictions using accuracy/balanced accuracy, confusion matrices, and calibration via reliability curves and Expected Calibration Error (ECE). Step 3 updates literature-derived CPTs using local datasets, with ML outputs and SHAP patterns contributing likelihood information for Bayesian updating, and hierarchical Bayesian modelling used to account for variability where appropriate. Step 4 proposes a Continuous Knowledge Integration Process (CKIP) to update the BN with new literature and real-time data streams. Integration across modules (N, irrigation, roots, VIs) calibrates the BN to site behaviour and supports operational outputs (e.g., irrigation volume, nitrogen rate, stress detection) with uncertainty propagation.

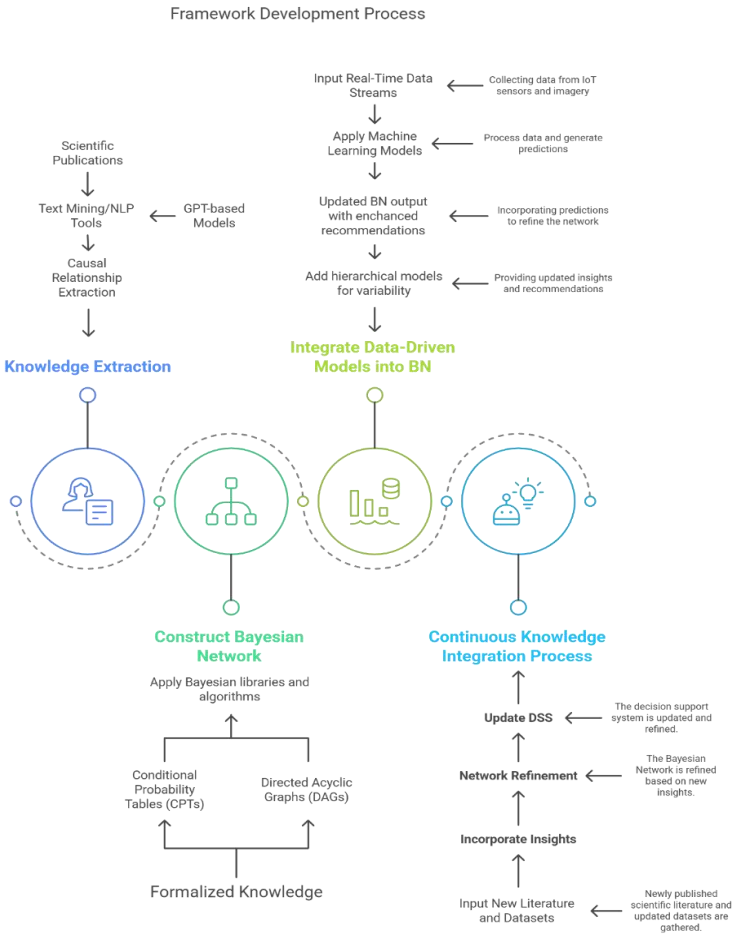
Framework Development Process
Scientific Publications
Text Mining/NLP Tools
GPT-based Models
Causal Relationship Extraction
Knowledge Extraction
Input Real-Time Data Streams
Collecting data from IoT sensors and imagery
Apply Machine Learning Models
Process data and generate predictions
Updated BN output with enchanced recommendations
Incorporating predictions to refine the network
Add hierarchical models for variability
Providing updated insights and recommendations
Integrate Data-Driven Models into BN
Construct Bayesian Network
Apply Bayesian libraries and algorithms
Conditional Probability Tables (CPTs)
Directed Acyclic Graphs (DAGs)
Formalized Knowledge
Continuous Knowledge Integration Process
Update DSS
The decision support system is updated and refined.
Network Refinement
The Bayesian Network is refined based on new insights.
Incorporate Insights
Input New Literature and Datasets
Newly published scientific literature and updated datasets are gathered.

3 Results

3.1 Part 1. Optimizing Nitrogen Fertilization and SOM dynamics

1) Vegetation indices, optimal lags, and composite signals (N and acc_N_rate)

A full lag scan (2–14 days) identified the strongest single VI associations with nitrogen variables. For applied fertilization rate **(N)**, **DVI at lag 2 days** produced the highest correlation (**r = 0.270**, $p < 0.001$). For accumulated nitrogen rate **(acc_N_rate)**, **GOSAVI at lag 5 days** was strongest (**r = 0.252**, $p = 0.003$). These lag windows likely reflect the time required for canopy properties (density, chlorophyll signal, green–brown contrast) to respond after fertilization and growth pulses.

When multiple VIs were combined into composites, the canopy signal strengthened. For **(N)**, both the lag-specific and GLOBAL composites produced slightly higher correlations (**r ≈ 0.30–0.32**) than the best single VI. For **acc_N_rate**, the GLOBAL composite consistently outperformed single VIs (**r = 0.342**, $p < 0.001$), indicating that integrating multiple canopy channels better represents cumulative growth and nitrogen removal.

Table 4. Highest Pearson correlations between VIs at lag windows (2–14 days) and the two nitrogen-related response variables: the fertilization rate (N) and accumulated nitrogen (acc_N_rate).

Top correlations with (N)			Top correlations with acc_N_rate		
Lag	**VI**	**Correlation with (N)**	**Lag**	**VI**	**Correlation with acc_N_rate**
2	DVI	0.270026	5	GOSAVI	0.251954
2	MSR	0.236140	4	GOSAVI	0.242078
4	MSR	0.204282	4	SAVI	0.235005
2	SAVI	0.170501	4	MSAVI	0.233556
10	MPRI	0.165335	7	GOSAVI	0.228355
14	MPRI	0.153311	2	DVI	0.227865
2	GOSAVI	0.132502	5	MSAVI	0.225554
8	MSR	0.121539	2	SAVI	0.224635
8	DVI	0.121521	5	SAVI	0.223829
7	GOSAVI	0.117007	6	MSAVI	0.220579

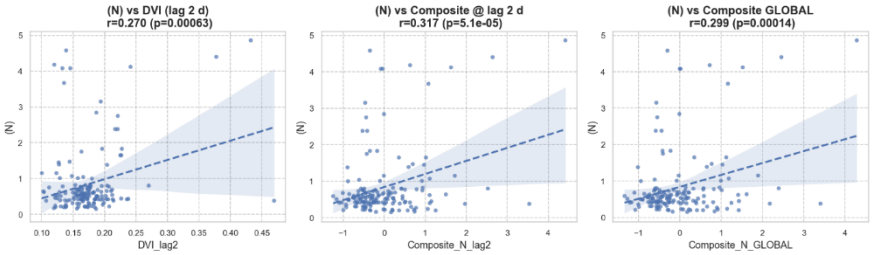

Figure 3. Relationships between fertilization rate (N) and (a) the best-performing single VI at its optimal lag (DVI_lag2), (b) the lag-specific composite index, and (c) the global composite index.

Composites show higher correlation coefficients ($r \approx 0.30–0.32$) than the single VI, indicating that combining spectral information improves representation of management-driven canopy responses.

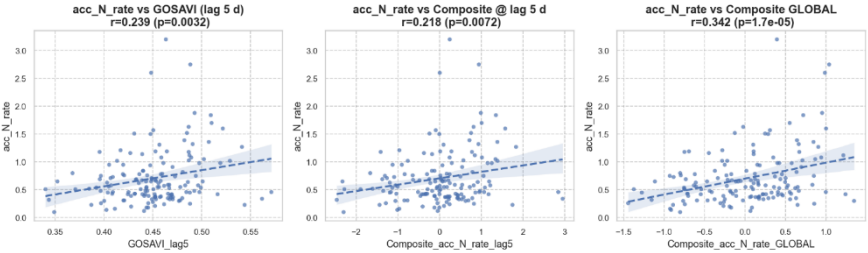

Figure 4. Relationships between accumulated nitrogen removal (acc_N_rate) and (a) the strongest VI (GOSAVI_lag5), (b) the lag-specific composite, and (c) the global composite. The global composite produces the highest correlation ($r = 0.342$, $p < 0.001$), reflecting the advantage of integrating multiple canopy signals to represent cumulative growth.

2) Baseline supervised prediction using VI features only (train 2023 → test 2024)

VI-only models captured seasonal patterns but tended to over-smooth abrupt transitions. For **(N)**, the best VI-only model was **Gradient Boosting** with **RMSE = 0.321** and **R^2 = 0.369**, meaning VIs alone explained ~37% of variance in manager-applied fertilization rate. For **acc_N_rate**, **HistGradientBoosting** performed best with **RMSE = 0.300** and **R^2 = 0.396**, showing that canopy state contains substantial information about cumulative clipping-related N removal.

Time-series evaluations for 2024 show that VI-only models generally track the seasonal trajectory but miss sudden changes (early-spring peaks; late-summer dips), motivating incorporation of environmental stress predictors.

Table 5. Predictive performance of models trained on 2023 VI features and tested on 2024. Gradient Boosting was most effective for (N).

(N) models (train 2023 → test 2024)			
Model	**Test RMSE**	**Test R^2**	**Notes**
Gradient Boosting	0.321	0.369	Best performer
Ridge	0.331	0.328	Stable linear baseline
HistGB	0.396	0.039	Underfits non-linearities
Random Forest	0.398	0.027	Over-smoothing
CatBoost	0.437	–0.17	Overfits train season

Table 6. Predictive performance of models trained on 2023 VI features and tested on 2024 HistGradientBoosting performed best for acc_N_rate.

acc_N_rate models (train 2023 → test 2024)			
Model	**Test RMSE**	**Test R^2**	**Notes**
HistGradientBoosting	0.300	0.396	Best performer
Ridge	0.331	0.265	Smooth linear baseline
CatBoost	0.336	0.243	Reasonable fit
Random Forest	0.337	0.242	Similar to CatBoost
Gradient Boosting	0.386	0.003	Essentially no predictive power

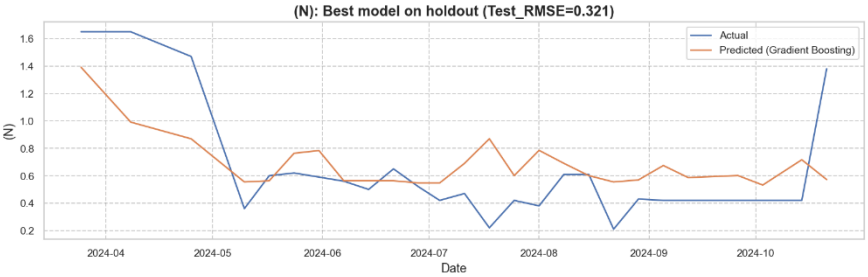

Figure 5. (N) Seasonal predictions for 2024 using VI-only models. Panels show that VI features capture the overall seasonal trajectories but miss abrupt transitions, especially early-season peaks and late-season declines. These limitations justify the inclusion of environmental stress predictors.

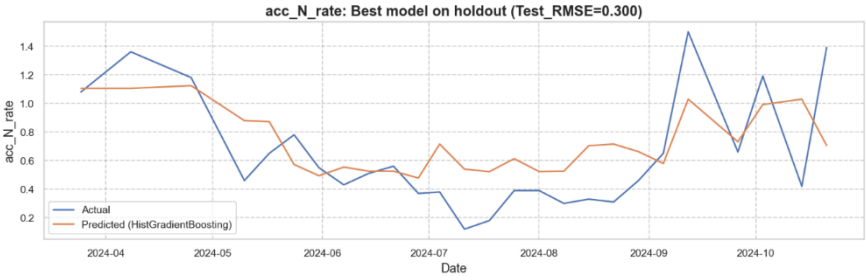

Figure 6. Acc_N_rate Seasonal predictions for 2024 using VI-only models. Panels show that VI features capture the overall seasonal trajectories but miss abrupt transitions, especially early-season peaks and late-season declines. These limitations justify the inclusion of environmental stress predictors.

3) Stress-wave signals are expressed in VIs (stress → canopy response)

To quantify the effect of environmental stress on canopy dynamics, drought/heat variables were derived from long-term weather records and tested across lag combinations. Among ~12,000 tested combinations, the strongest single relationship was **DVI vs deficit3 at lag 2 days** (**r = 0.258**, p = 0.001), indicating that short precipitation–ET deficits suppress greenness/contrast indices within ~1–3 days. Similar patterns were observed for structure-sensitive VIs such as SAVI.

When summarised by VI, the best stress descriptors differed by index (examples: DVI best aligned with deficit3 at lag 2; EXG aligned with heat_flag at lag 1; chlorophyll-sensitive indices aligned with longer heat-wave length at lag 14), confirming that stress information is detectably encoded in spectral signals in a physiologically coherent direction.

Table 7. Strongest correlations between environmental stress descriptors and VIs across lag windows

Best stress feature per VI				
VI	**Lag**	**Stress feature**	**r**	**Interpretation**
DVI	2	deficit3	0.258	Canopy contrast drops after short-term water imbalance
EXG	1	heat_flag	0.169	Heat reduces green dominance
GBNDVI	14	heat_wave_len	0.213	Long heat waves increase drying/necrosis signal
GNDVI	14	heat_wave_len	0.226	Heat influences chlorophyll-sensitive indices

4) Full models with lag-aligned stress predictors (VI + stress), and interpretable drivers

Stress metrics were aligned to the optimal VI lags (stress at t−L predicting VI_lagL and the response at t). Only the top-K stress features (K = 6) were included (ranked by association with the target in the training season). For **(N)**, the best model was **Ridge Regression** with **RMSE = 0.272** and **R^2 = 0.548**, a substantial improvement relative to VI-only performance ($R^2 \approx 0.37$). This indicates that fertilization decisions were more tightly linked to recent heat/moisture stress conditions than to canopy reflectance alone.

The standardized coefficients show that **deficit3_aligned_lag2** was the strongest predictor, followed by short-term heat accumulation (heat_dd7_aligned_lag2; heat_dd3_aligned_lag2) and longer drought-wave terms (drought_sum14_aligned_lag2; deficit14_aligned_lag2). Spectral predictors (DVI_lag2 and Composite_N_lag2) remained contributory but secondary to stress metrics.

For **acc_N_rate**, the best model was **HistGradientBoosting** with **RMSE = 0.294** and **R^2 = 0.422**, broadly comparable to VI-only performance ($R^2 \approx 0.40$) but with improved robustness early in the season. Feature importance differed from (N): the **global composite** (Composite_acc_N_rate_GLOBAL) dominated, while **7–14 day deficits** (deficit7/14 aligned to lag 5) and longer drought sums modulated cumulative uptake, consistent with physiological control of clipping yield over medium time windows.

A compact summary of error reduction shows that incorporating aligned stress features reduced 2024 test RMSE from **~0.32 to ~0.27–0.29 for (N)** and from **~0.30 to ~0.27–0.29 for acc_N_rate**, supporting the view that fertilization patterns are strongly modulated by heat and drought stress that VIs alone cannot represent.

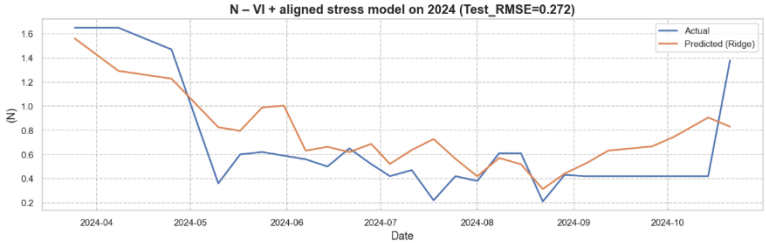

*Figure 7. (N) Seasonal predictions for 2024 using VI + assigned stress models. Panels show that VI features has a substantial improvements (R^2 = **0.548)** over VI-only models(R^2 = 0.37).*

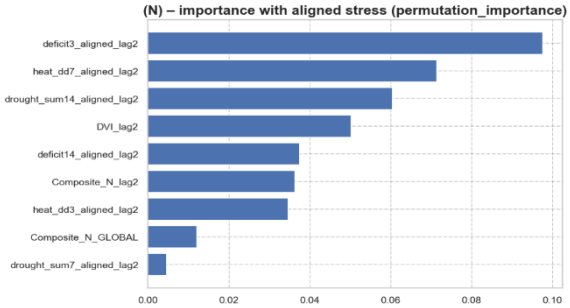

Figure 8. Standardized coefficients from the best-performing Ridge Regression model predicting fertilization rate (N). Short-term moisture deficits (deficit3_aligned_lag2) and heat accumulation (heat_dd7_aligned_lag2, heat_dd3_aligned_lag2) are the most influential predictors. Spectral variables contribute secondarily after stress metrics.

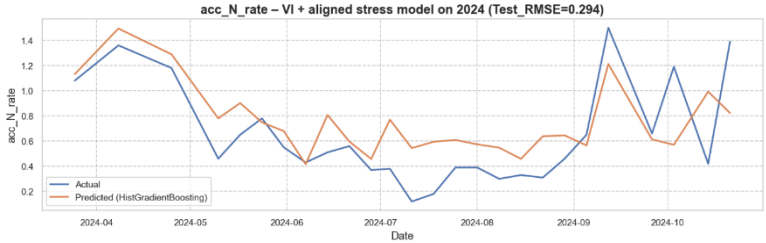

Figure 9. Predictions for 2024 using models that combine VIs with lag-aligned stress features. Incorporating heat and drought metrics improves responsiveness to early-season changes and reduces over-smoothing seen in VI-only models

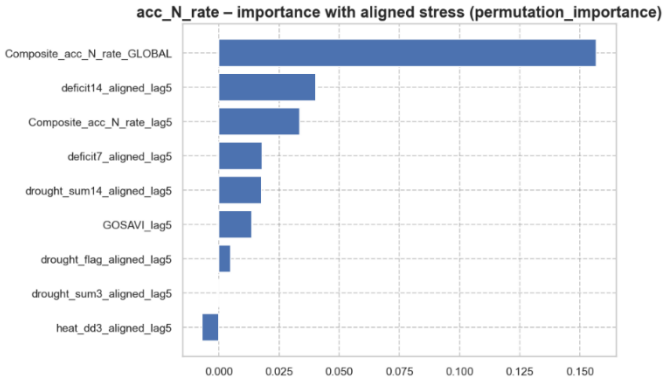

Figure 10. Feature importance from the HistGradientBoosting model predicting accumulated nitrogen removal (acc_N_rate). The global composite VI is the dominant predictor, while medium-term water deficits over 7–14 days strongly influence cumulative GP and clipping removal.

Table 8. VI only to VI+stresss RMSE comparison

Target	VI-only RMSE	VI+Stress RMSE	Meaning
(N)	~0.32	~0.27–0.29	Better tracking of fertilization triggers
acc_N_rate	~0.30	~0.27–0.29	Better representation of cumulative response

5) SHAP confirmation of the causal hierarchy (fast-cycle stress control vs canopy state)

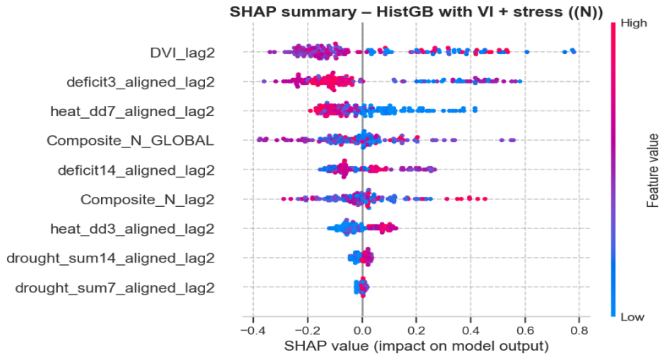

Figure 11. SHAP summary plot for the fertilization rate model (N) integrating VIs and lag-aligned environmental stress metrics

SHAP analyses supported the same hierarchy. For **(N)**, the strongest contributors were **deficit3_aligned_lag2** and **heat_dd7_aligned_lag2**, followed by longer drought signals.

Spectral features (DVI_lag2 and composites) provided stable but secondary contributions. For **acc_N_rate**, the dominant driver was **Composite_acc_N_rate_GLOBAL**, with medium-term water imbalance features (deficit and drought sums at 7–14 days) also influential; short acute stress events had minor contributions.

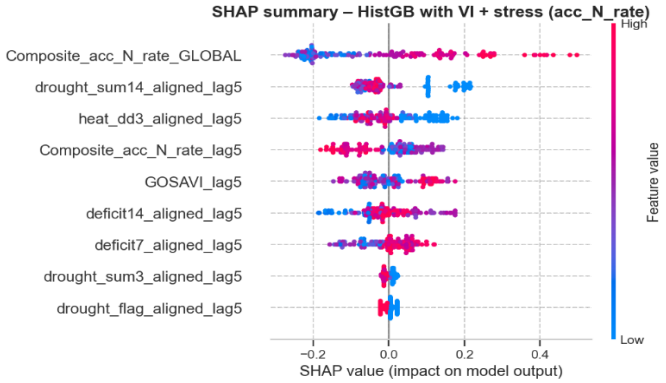

Figure 12. SHAP summary plot for the accumulated nitrogen removal model (acc_N_rate) using vegetation composites and aligned stress metrics

6) SOM dynamics (2019–2024): depth trends, N association, and AOI separation

Table 9. SOM belongs to carbon budget and is influenced by direct physical and indirect management drivers and represented by spectral signals.

Direct physical drivers	Indirect management drivers	Spectral signals
thatch accumulation	irrigation strategy	vegetation density
clipping inputs	N plan	NDVI/NDRE → biomass / canopy
root biomass	clipping removal	thickness
soil moisture regime	frequency	DGCI/EXG/VARI → chlorophyll &
decomposition environment	topdressing	color
(temperature, moisture,	stress-wave patterns	composite VIs → yield potential over
oxygen)	(heat, deficit)	time

SOM was monitored annually at three depths (0–25, 25–50, 50–75 mm) across four AOIs (p01, p10, pt1, pt2) over six years. Across AOIs, **SOM generally declined** at all depths except the high-N zone **pt2**, with the strongest decline in surface layers. SOM_1 decreased from **~9–10% (2019) to ~4–6% (2024)** (steepest in p01 and pt1), SOM_2 declined from **~7–8% to ~4–6%**, and SOM_3 decreased more slowly, stabilizing near **~2.0–2.8%**. AOI ranking persisted across depths (**pt2 > p10 > p01 > pt1**), consistent with sustained fertilization supporting higher OM levels under sand-based greens.

Annual total N input showed a strong positive association with SOM at all depths: **r ≈ 0.70 (SOM_1)**, **r ≈ 0.79 (SOM_2)**, **r ≈ 0.80 (SOM_3)**. This pattern is consistent with higher productivity supporting OM inputs through shoot density, clipping biomass, root turnover, and rhizosphere C deposition.

SOM co-varied strongly across depths (**SOM_1–SOM_2 r = 0.93; SOM_2–SOM_3 r = 0.90; SOM_1–SOM_3 r = 0.78**), suggesting shared long-term controls related to biomass inputs and management regime. Machine learning and SHAP were not applied to SOM due to the limited annual dataset size (n = 24 across depths and AOIs), and the further reduction when merging with root/clipping/thatch metrics.

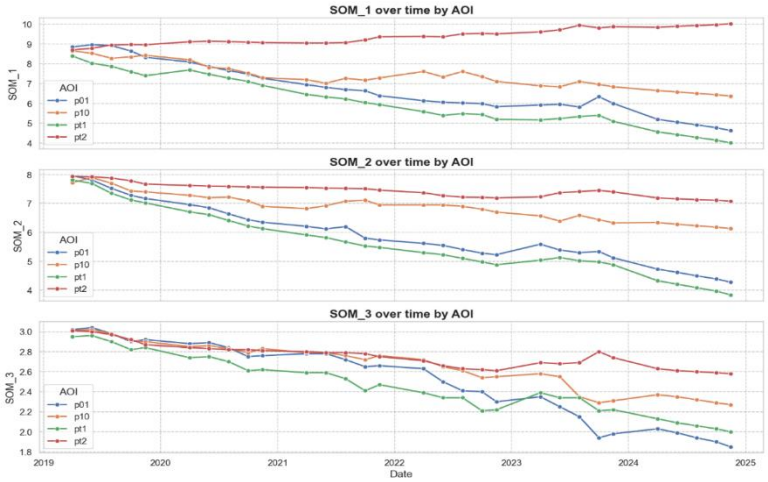

Figure 13. Temporal trends of soil organic matter (SOM) across three depths (0–25 mm, 25–50 mm, 50–75 mm) within four AOIs from 2019 to 2024. All areas except pt2 show declining SOM across depths, reflecting long-term dilution and decomposition in sand-based putting greens.

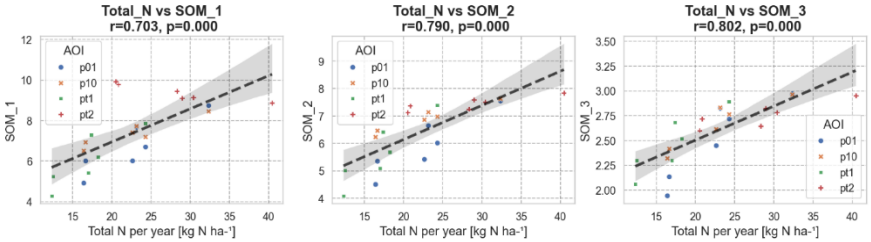

Figure 14. Relationships between annual nitrogen input and SOM at three depths. Strong positive correlations (r = 0.70–0.80) indicate that higher nitrogen fertilization supports SOM accumulation through increased shoot density, root turnover, and rhizosphere carbon deposition.

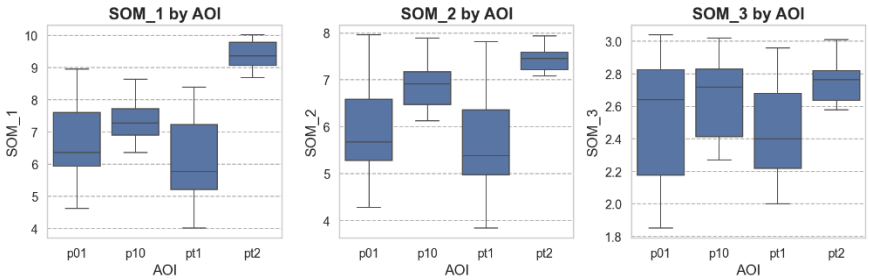

Figure 15. SOM distributions across AOIs at three depths. The +25% N treatment (pt2) consistently shows the highest SOM, while the −25% N treatment (pt1) maintains the lowest values, validating the expected treatment gradients

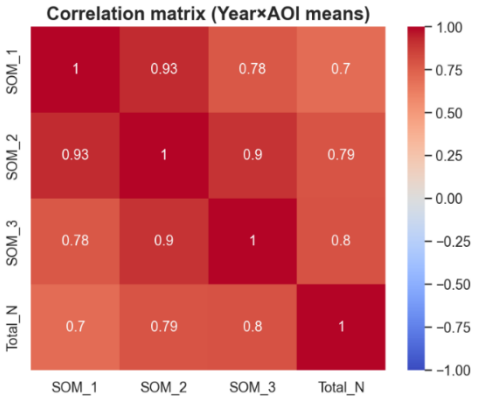

Figure 16. Correlation matrix showing co-variation of SOM across three depths. Strong correlations (r = 0.78–0.93) suggest common long-term controls related to biomass inputs, management regime, and moisture environment.

Together, the nitrogen modelling and SOM results define the core of the DSS nitrogen module: **fast-cycle** nitrogen dynamics (N and acc_N_rate) are governed by a coupled signal where canopy condition captures realized growth, while aligned stress metrics provide the missing environmental constraints that control short-term decisions and seasonal deviations. SOM acts as a **slow-cycle** sustainability indicator integrating multi-year outcomes of those decisions.

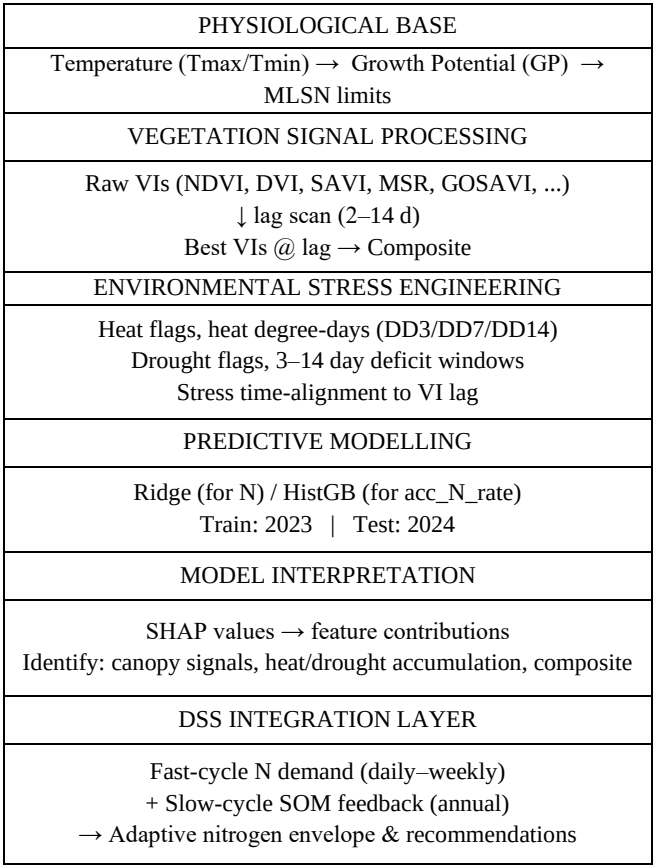

Figure 17. The diagram illustrates the central nitrogen–carbon feedback mechanism identified in this study. Nitrogen fertilization drives canopy density and clipping production, which in turn influence root growth and OM deposition. These inputs accumulate slowly into SOM. SOM then feeds back into the DSS as a long-term sustainability indicator, modifying the recommended nitrogen envelope for subsequent seasons. This forms a closed loop connecting short-term N demand with long-term carbon storage.

3.2 Part 2. Irrigation optimization

1) GCA (2019–2024): temporal soil moisture dynamics and irrigation performance

Multi-year stress classification (FAO56 SWB). The FAO56-style soil water balance reconstructed for GCA (2019–2024) shows a highly stable seasonal pattern: the putting green remains predominantly in **moderate stress** for most of the growing season, typically **~170–180 days/year**, while **no-stress** conditions occur for **~55–65 days**, depending on rainfall distribution. **High-stress days are nearly absent** under the current irrigation strategy. This indicates a managed regime that routinely permits partial depletion without entering severe stress, but it also implies sensitivity to short under-irrigation periods during peaks in ETc. (Figure 38)

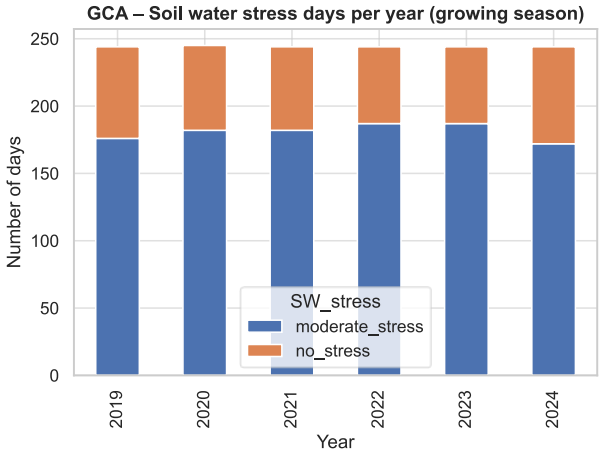

Figure 18. Soil water stress days per year (GCA, 2019–2024). Annual counts of days classified as no-stress, moderate-stress, and high-stress based on the FAO56 soil-water-balance reconstruction. Moderate stress consistently dominated the seasonal moisture regime (≈170–180 days per year), while high-stress conditions were nearly absent.

VWC response to net daily water balance (P + I − ETc). Across years, most observations fall within a narrow VWC band of **~18–28%**, consistent with the limited water-holding capacity of the sand profile and frequent low-volume irrigation. Negative (P+I−ETc) values are associated with VWC decline, but the response is non-linear due to frequent irrigation events and rapid drainage. Positive water balance does not increase VWC proportionally above **~28–30%**, implying an operational field-capacity ceiling where additional water drains below the sensor depth and becomes non-beneficial for next-day VWC. These patterns directly support moisture-state thresholds for the DSS around **<18% (depletion-prone)**, **18–26% (optimal band)**, and **~28% (drainage/non-beneficial zone)**..

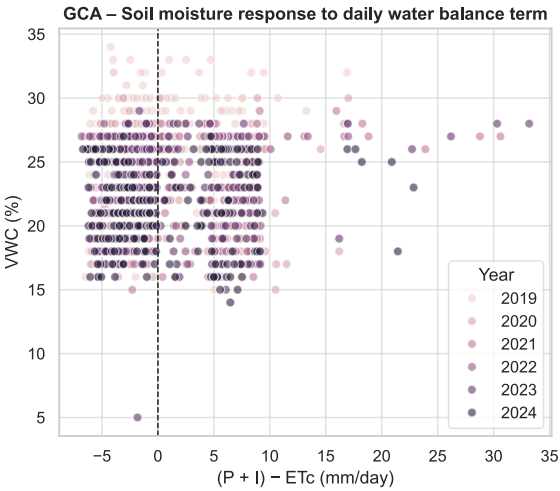

Figure 19. Soil moisture response to the daily water-balance term (P + I − ETc). Relationship between TDR-measured VWC and net daily water balance. Negative balance values correspond to moisture decline, while positive values plateau near 28–30% VWC, indicating the practical field-capacity limit of the sand profile. The narrow VWC range reflects rapid drainage and the stabilizing effect of frequent low-volume irrigation.

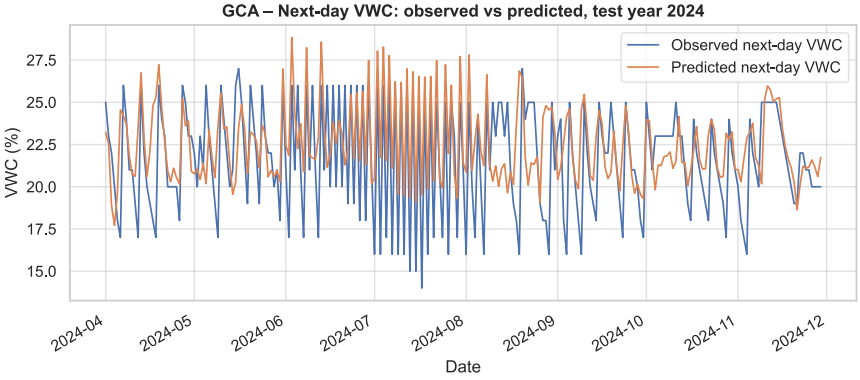

Figure 20. The time-series view for 2024 confirms that the model tracks the general drying/wetting cycles (daily oscillation patterns) even though individual peaks and troughs are not perfectly aligned. This is expected given the high-frequency noise and the sensitivity of sand-based greens.

Next-day VWC prediction (ML). A **GradientBoostingRegressor** was identified as the best-performing approach for next-day VWC prediction. Predictive accuracy is described as

practically useful for decision-making in a sand green, with **RMSE in the ~2–3% VWC range**, and moderate but stable generalisation to test conditions. Scatter and time-series views indicate good tracking of wetting-drying cycles with expected limitations at extremes: slight underestimation at very high VWC and increased variability at low VWC (<18%), reflecting rapid drying under high ETc. (Figure 40)

SHAP driver hierarchy and threshold behaviour. SHAP interpretation confirms a physically coherent hierarchy:

1. **Current VWC** is the dominant predictor (strong inertia of soil moisture).
2. **ETc** is the second most influential driver, with clear threshold-like behaviour: **ETc < ~2 mm/day** yields minor drying; **ETc ~3–5 mm/day** progressively reduces next-day VWC; **ETc > ~5.5 mm/day** produces strong negative contributions consistent with rapid drying peaks.
3. **DOY** captures seasonality.
4. **Precipitation and RH** provide stabilising positive effects.
5. Temperature terms act mainly through ETc/VPD, while drought flags and depletion indices add context, especially under medium-to-low moisture states. (Figure 41, 42a, 42b, 43, 44)

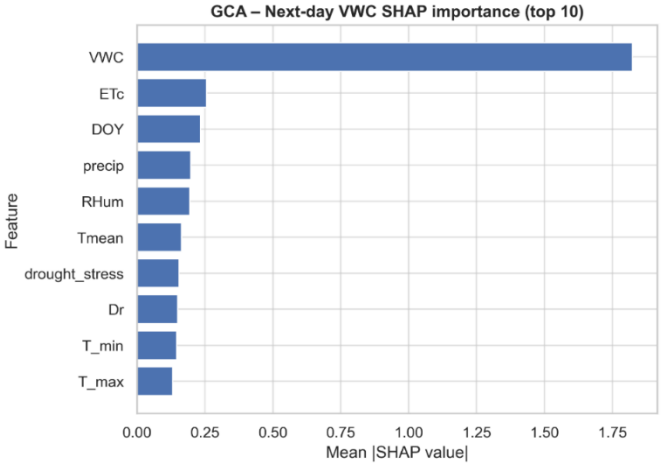

Figure 21. Top-10 SHAP feature importance for next-day VWC. showing the relative mean absolute SHAP contribution of each predictor. VWC overwhelmingly dominate prediction behavior, confirming the strong inertia and climatic dependence of moisture in a sand green

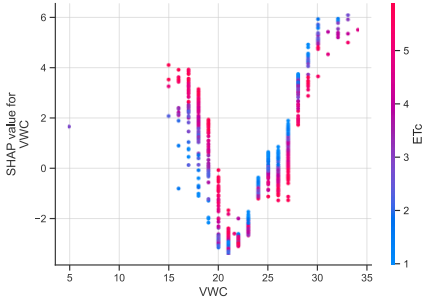

Figure 22a SHAP dependence for current VWC in the next-day VWC model (GCA), coloured by ETc. Contributions are most negative around ~20–22% VWC and become more positive at lower and higher VWC; higher ETc generally shifts values downward.

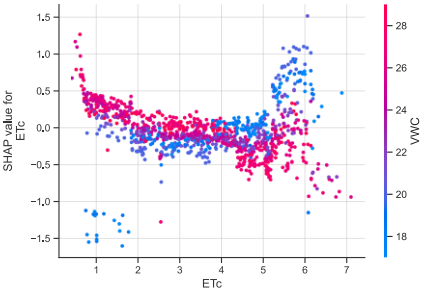

Figure 42b SHAP dependence for ETc in the next-day VWC model (GCA), coloured by current VWC. Increasing ETc tends to reduce next-day VWC, with stronger and more variable effects at ~5–6+ mm day⁻¹ depending on starting moisture.

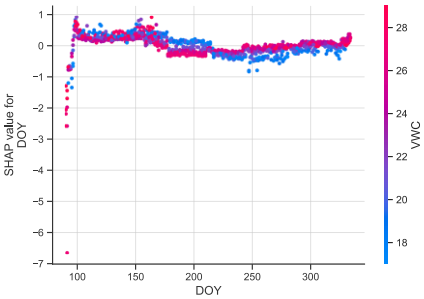

Figure 23 SHAP dependence for DOY (coloured by current VWC) in the next-day VWC model (GCA), showing seasonality: early DOY tends positive, mid-season (≈190–280) slightly negative, late season near-neutral to mildly positive.

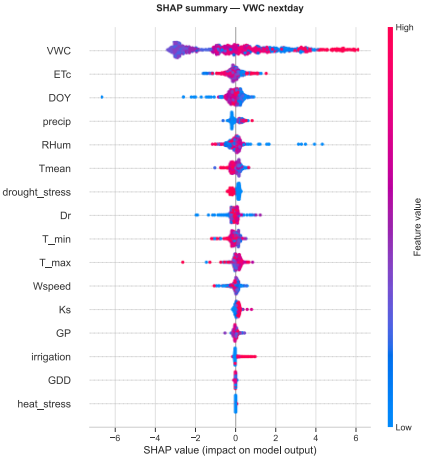

Figure 24 SHAP summary (beeswarm) for the next-day VWC model (GCA). VWC is the main driver, followed by ETc and DOY; precipitation and RH are secondary. Colour indicates low-to-high feature values

Operational thresholds extracted from combined analyses. The combined descriptive, predictive, and SHAP analyses converge on decision thresholds:

- **Optimal VWC band: 18–26%** (stable dynamics, neutral SHAP behaviour).
- **Lower limit: ~16–18%** (sharp negative SHAP, fast decline when ETc > ~4 mm/day; practical "start irrigation" trigger).

- **Upper limit: ~28–30%** (VWC plateaus; diminishing returns; avoid unnecessary irrigation).
- **ETc state thresholds:** <2, 3–5, >5.5 mm/day (Low/Medium/High evaporative demand nodes).

These thresholds are directly suitable for discretisation into BN node states for irrigation decisions.

2) GCB (2024): spatial soil-moisture patterns across greens (S_3, S_4, W_9)

Seasonal dynamics of spatial uniformity. Weekly VWC grids for 2024 were used to quantify within-green moisture distribution and temporal stability. **DU** improved from early May to mid-season and stabilised above the commonly accepted **DU = 0.75** threshold. S_4 maintained consistently high DU (~0.85–0.92 after mid-May), while S_3 and W_9 showed stronger early-season variability (W_9 increasing rapidly from ~0.65 to ~0.90 after initial dates). (Figure 45)

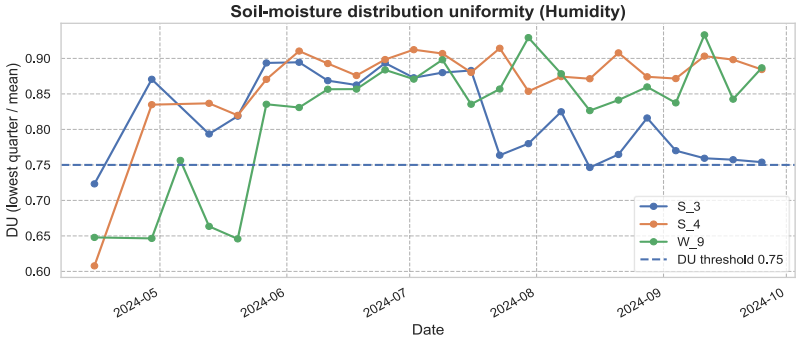

Figure 25. Seasonal trends in distribution uniformity (DU) for S_3, S_4, and W_9. DU increases from early spring toward mid-season across all greens, stabilizing above the acceptable threshold (DU = 0.75). S_4 maintains the highest DU throughout the season, while S_3 and W_9 show greater early-season variability.

Spatial variability (CV). CV patterns complement DU by describing heterogeneity intensity. S_4 remained most stable (**~8–12%**), whereas S_3 and W_9 exhibited pronounced early-season variability (peaks around **~20–23%**) and, for S_3, an additional late-summer variability peak (~22%) consistent with DU decline. (Figure 46)

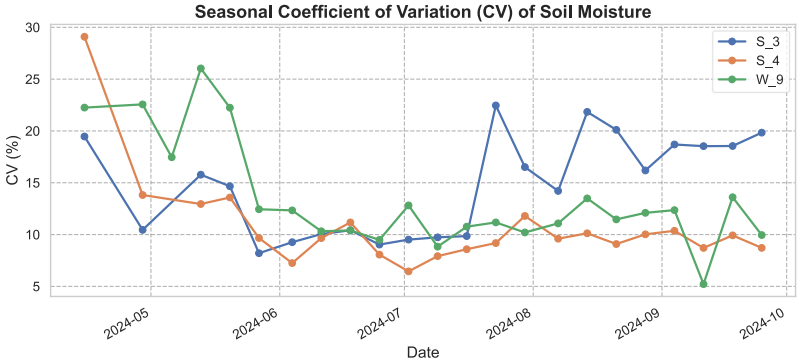

Figure 26. Seasonal coefficient of variation (CV) of VWC for S_3, S_4, and W_9. CV patterns reveal spatial heterogeneity and complement DU interpretation. S_4 exhibits consistently low CV (≈8–12%), while S_3 and W_9 show substantial early-season variability and localized heterogeneity later in the season.

Moisture-state area fractions (Dry/Optimal/Wet). Classifying grid points into Dry, Optimal, and Wet states shows that **Optimal conditions dominate** across greens, with Dry conditions appearing episodically (early/late season or during temporary declines in uniformity). Wet patches were generally limited and short-lived, except early in W_9 and at periods in S_3. The three greens are best presented with one figure per green. (Figures 47–49).

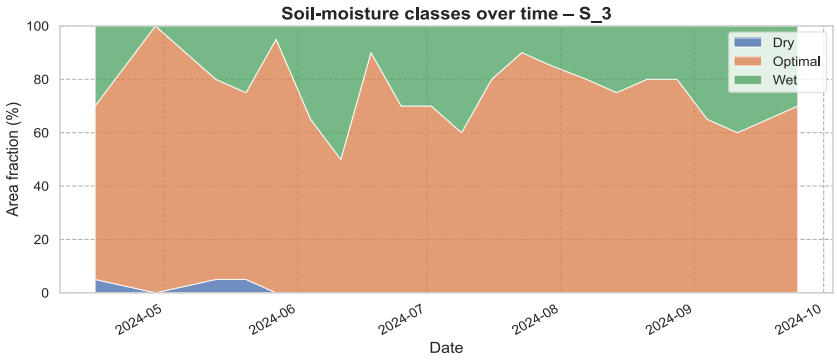

Figure 27. Proportion of Dry, Optimal, and Wet areas over the season for S_3.

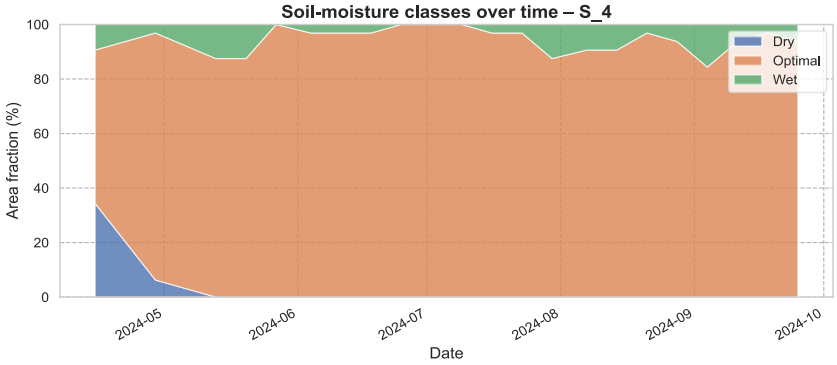

Figure 28. Proportion of Dry, Optimal, and Wet areas over the season for S_4.

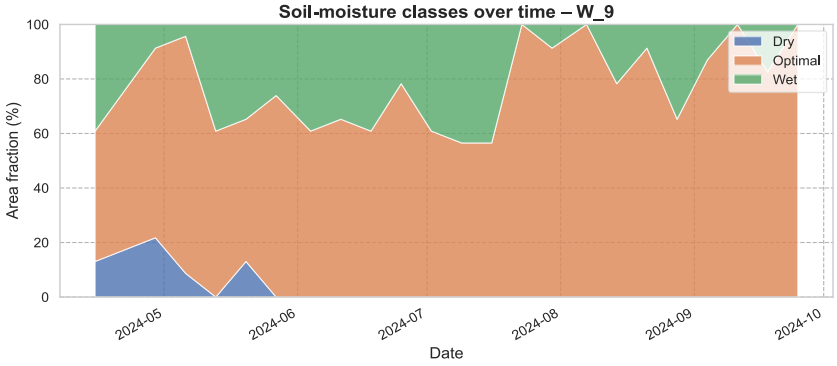

Figure 29. Proportion of Dry, Optimal, and Wet areas over the season for W_9.

Persistent zones via time-series clustering (k-means, k=3):

- Persistent dry zones (potential hydrophobic pockets, sprinkler shadowing/wind exposure).
- Transient zones (normal response to irrigation/rain).
- Persistent wet zones (micro-depressions, overlap, drainage constraints, shade/compaction).

  S_3 shows notable persistent dry zones (left and lower-central) plus small wet pockets near perimeter, aligning with its late-season DU decline. S_4 is largely transient/wet with minimal persistent dry points, consistent with best DU/CV performance. W_9 has stable but smaller wet and dry pockets with transient dominance. (Figures 50–53)

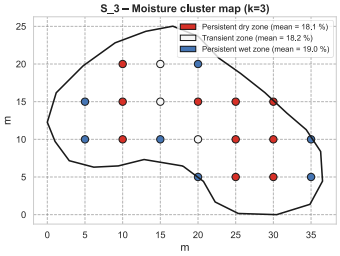

Figure 30. Moisture-cluster map for S_3 using k-means (k = 3).

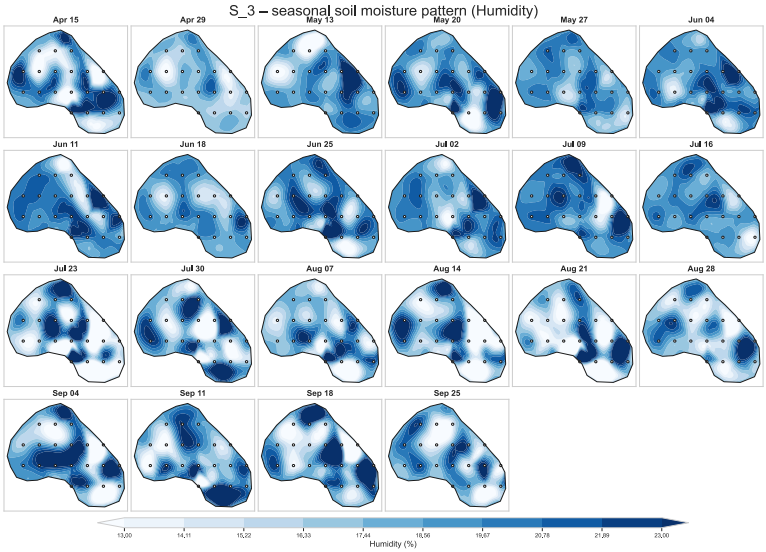

Figure 31. Example of seasonal moisture clustering for S_3

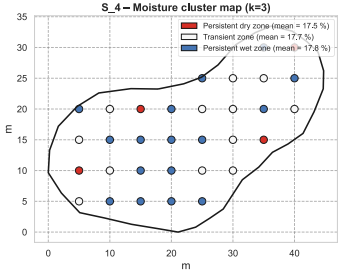

Figure 32. Moisture-cluster map for S_4 using k-means (k = 3)

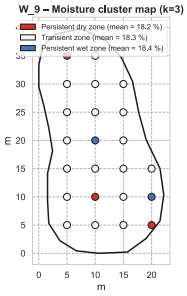

Figure 33. Moisture-cluster map for W_9 using k-means (k = 3).

3) Integration into the SMART-DSS irrigation module (temporal + spatial)

INTEGRATED IRRIGATION INTELLIGENCE FRAMEWORK (GCA + GCB)		
INPUT LAYER		
Weather Data PAR, Tmin, Tmax, RH Wind, solar radiation Rainfall, ET_0 (PM)	Management Data Irrigation (D / WD) ET-based scheduling Fertilization Mowing / clipping	Soil & Spatial Data TDR VWC (GCA, daily) Weekly VWC grids (GCB) Green boundary polygons DU, CV, moisture classes
TEMPORAL - SPATIAL ANALYSIS LAYER		
GCA: TEMPORAL WATER BALANCE	GCB: SPATIAL MOISTURE PATTERNS	
$ETc = ET_0 \times Kc$ Daily water balance: Irrigation + Rain − ETc Stress indicators: Soil Water Deficit (SWD), Ks, DS, stress classes Efficiency metrics: WUE, IWUE, HUE Seasonal patterns: VWC dynamics, ET demand	VWC heatmaps (interpolated surfaces) Spatial indices: DU, CV Moisture-class area fractions: Dry / Optimal / Wet Cluster analysis (k=3): Persistent dry zones Transient zones Persistent wet zones Spatial stability across season	
SYNTHESIS OF TEMPORAL + SPATIAL BEHAVIOR		
Rising ETc deficit → temporal stress (GCA) Chronic dry pockets → spatial under-irrigation (GCB) High CV or low DU → uneven irrigation distribution	High wet-area fraction → potential over-irrigation / drainage issue Stable clusters → strong spatial priors Unstable clusters → higher DSS uncertainty weight	
SMART-DSS IRRIGATION MODULE (OUTPUT LAYER)		
Feature Engineering for BN		
Temporal Features (GCA):	Spatial Features (GCB):	
Rolling ET deficit Time since last effective rainfall Daily VWC stress state Predicted next-day VWC (ML model) Seasonal phase classification	DU class (High / Medium / Low) CV class (Stable / Variable / Highly variable) Cluster identity (Dry / Transient / Wet) Moisture-class area fractions Persistent zone flags (dry/wet) Spatial uncertainty factor	
BN / CPT Integration		
Convert thresholds → discrete BN nodes Populate CPTs using empirical seasonal behavior Combine temporal + spatial indicators	Output → risk-adjusted irrigation recommendation: Increase irrig: ET deficit+dry cluster+low DU Decrease irrigation: wet cluster+low ET Alert: persistent wet zones / low DU / unstable	

Figure 34. Integrated temporal–spatial irrigation framework for the SMART-DSS.

Part 2 integrates a temporal rule set from GCA with a spatial diagnostic layer from GCB. GCA defines the dynamic response: moisture inertia (VWC_today), ETc-driven depletion rate, and a practical moisture window (**18–26%**) bounded by depletion-prone and non-beneficial zones. GCB defines spatial modifiers: DU, CV, moisture-class area fractions, and persistent dry/wet clusters that explain why stress or saturation can occur locally even when whole-green averages appear acceptable. In the DSS, temporal nodes (VWC_today, ETc_today, net balance, short-term drought accumulation, predicted next-day VWC) drive base irrigation decisions, while spatial nodes (uniformity/heterogeneity/zone identity) adjust risk and confidence and support targeted remediation (nozzle tuning, aeration, wetting agents, local drainage corrections).

3.3 Part 3. Root system development

After establishing in Part 1 that growth and nitrogen dynamics are strongly modulated by short-term stress, and in Part 2 that VWC and ETc thresholds control the depletion-recovery cycle on sand-based greens, Part 3 focuses on the biological "receiver" of those decisions: the root system. The results below quantify seasonal root-length trajectories under contrasting irrigation regimes, then extend them into spatial, management, and remote sensing proxies that can be operationalised in the SMART DSS.

1) Seasonal root-length dynamics under Daily (D) vs Water-Deficit (WD) irrigation (2023–2024)

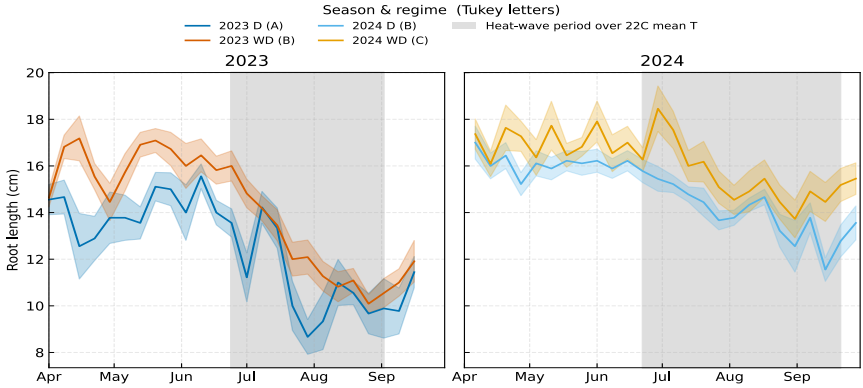

Figure 35. Seasonal root-length dynamics under daily (D) and water-deficit (WD) irrigation (2023–2024). ime-series of root length showing consistent spring increases to 15–18 cm, followed by summer decline.

Across both years, root length followed a consistent seasonal trajectory: **spring increase (April to June) toward peaks around 15–18 cm**, followed by a **progressive summer decline (July to September)**. WD consistently produced deeper roots than D, with clearer

separation early in the season and sustained advantage during stress periods. Heat-wave periods (shaded) align with the onset of accelerated decline, with **D showing sharper mid-summer collapse**, particularly in 2023, while **WD reduced the rate of decline and maintained longer functional roots** during the heat-wave window. Partial recovery occurs after peak stress but does not return to spring maxima, matching a typical C3 seasonal rooting pattern under summer stress.(Figure 55)

2) Mixed-effects model and treatment hierarchy (statistical confirmation)

The mixed-effects model confirmed that **2024 roots were significantly longer than 2023** (approximately **+2.40 cm**, **$p < 0.001$**). The **Season × Irrigation** interaction was **not significant ($p = 0.29$)**, indicating that the WD advantage was stable across years rather than being year-dependent. The Tukey compact-letter display provides an interpretable ranking of groups:

- **2023-D**: shortest roots
- 2023-WD and 2024-D: intermediate
- **2024-WD**: deepest

This establishes a clear management ladder in the dataset:

Daily irrigation (shallowest) → Water deficit (deeper) → Water deficit plus more favorable season (deepest).

Table 10. Mixed-effects model summary for root length across seasons and irrigation regimes. Fixed-effect estimates indicating that 2024 roots were significantly longer than 2023 roots, the irrigation main effect was modest when examined alone, and the Season × Irrigation interaction was non-significant. The seasonal improvement and irrigation-driven differences are captured more clearly in group means than in raw coefficients, due to model centering.

Effect	Interpretation
Season (2024 > 2023)	2024 had significantly longer roots overall (~+2.40 cm, $p < 0.001$), consistent with cooler early-season conditions and slightly lower ET demand.
Irrigation main effect	The WD vs. D difference was detectable but not statistically large as a main effect-because the interaction captures most of the variation.
Season × Irrigation interaction	Not statistically significant ($p = 0.29$), meaning the WD advantage was **consistent across years**, not dependent on season.

Table 11. Tukey compact-letter display (CLD) for treatment-based root-length groupings

Group	Treatment	Interpretation
A	2023-D	Shortest roots
B	2023-WD, 2024-D	Intermediate depths
C	2024-WD	Deepest roots

3) Spatial structure across AOIs, separated by irrigation regime and fertilisation (GP, GP+25%, GP−25%)

Root-length distributions across AOIs show strong spatial structure on the putting green. One-way ANOVA indicates a highly significant **AOI effect ($F_{19,1000} = 10.0$, $p < 0.001$)** and a highly significant **year effect ($F_{1,1018} = 142.3$, $p < 0.001$)**, consistent with the seasonal model results. In the AOI violin and boxplot view, WD zones generally shift toward deeper roots relative to D zones, while fertilisation intensity modulates the envelope of root-length distributions. In this dataset, **pt1 (GP+25%)** tends toward the shallowest distributions and **pt2 (GP−25%)** toward the deepest, while most GP areas occupy an intermediate band. This spatial view complements the time-series: the D versus WD separation persists across the whole sampling domain and is not only a transient seasonal phenomenon.

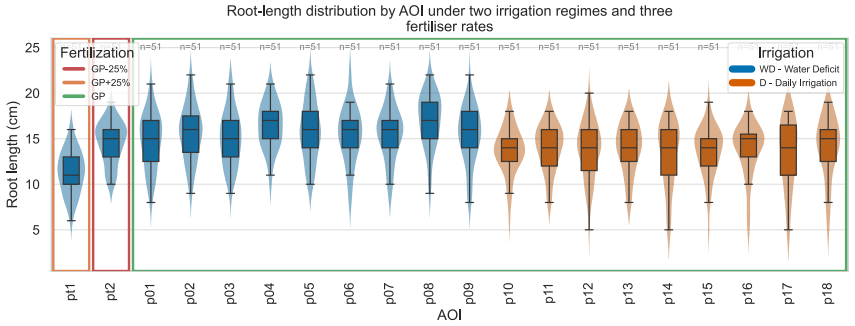

Figure 36. Spatial distribution of root length across AOIs, irrigation regimes, and fertilisation treatments. Violin + boxplots showing the full distribution of root lengths across the green. WD zones generally exhibit deeper roots than D zones, while fertilisation intensity (GP−25 %, GP, GP+25 %) modulates the lower and upper extremes.

4) Year-by-year treatment responses by irrigation × fertilisation (distribution view)

When the data are regrouped by year and fertilisation level (GP+25%, GP, GP−25%) and separated by irrigation regime, medians rise in most facets from **2023 to 2024**, confirming that the year effect is robust across management strata. Within each fertilisation level, WD tends to maintain **equal or greater** root length than D, with the WD advantage most visible in 2024. Under **GP−25%**, WD maintains relatively deep roots with a narrower IQR, suggesting a more constrained but stable root system under combined N and water savings. Together, this block supports empirically defined "root-length envelopes" per management combination for DSS use.

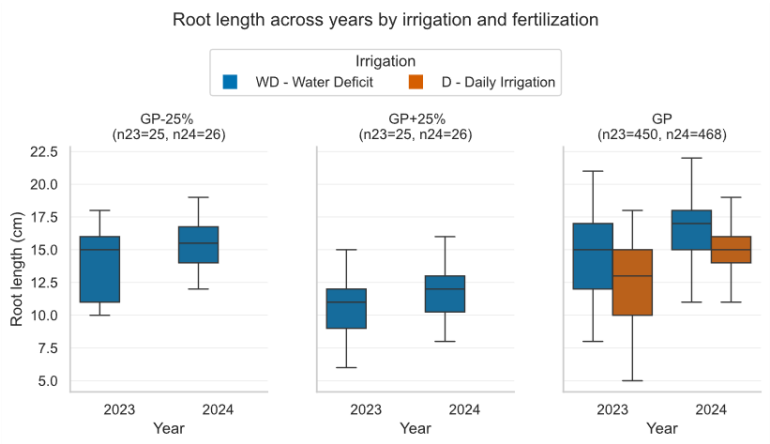

Figure 37. Year-by-year root-length responses by irrigation regime and fertilisation level. Faceted boxplots comparing 2023 and 2024, grouped by fertilisation strategy.

5) Remote sensing proxy- single lagged vs composite VI for tracking root length (WD vs D)

Single lagged VIs show meaningful associations with root length in both irrigation regimes, with relationships distributed across several indices and lags rather than concentrated in one VI. The best single VI–lag per regime provides a useful baseline spectral proxy, confirmed visually by regression scatterplots with confidence bands.

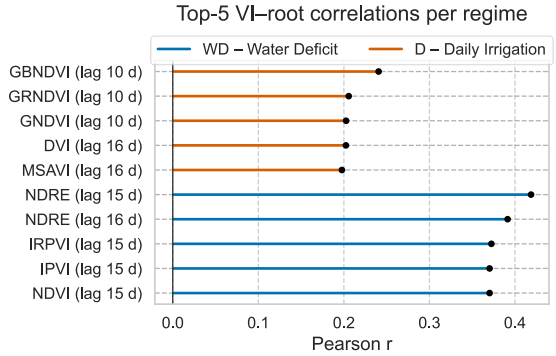

Figure 38. Ranked correlations of single lagged VIs with root length under WD and D irrigation regimes. Forest plot showing the strongest |r| values for each irrigation regime. Multiple lagged VIs exhibit meaningful associations with root length, confirming that belowground dynamics can be partly inferred from delayed canopy responses

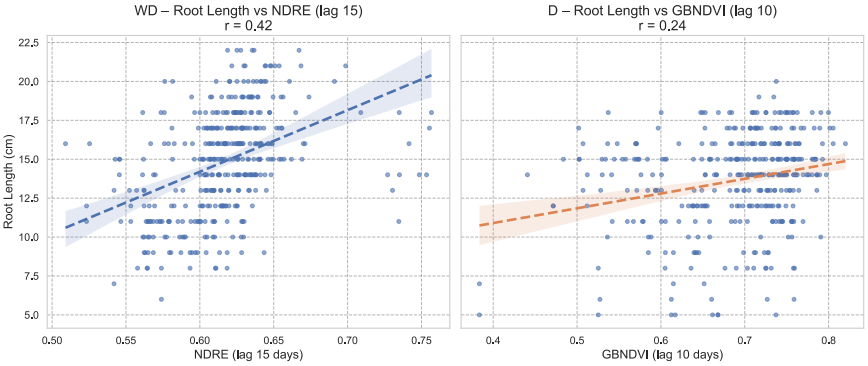

Figure 39. Scatterplots of root length versus the best single VI–lag combination for each irrigation regime. Regression plots (with 95% CIs) illustrating the strongest single spectral predictors of root length for WD and D. Both show clear monotonic relationships, with tighter clustering under D and greater variability under WD.

A greedy composite procedure combining multiple VI–lag pairs increased |r| most strongly when moving from **k = 1 to k ≈ 2–3**, after which gains plateaued or diminished. The best composites achieve correlations that are at least as strong, and typically slightly stronger, than the best single VI. Weight profiles show that only a small subset of VIs carries most influence within each composite, supporting a parsimonious design (small composites are sufficient). The marginal gain curve (Δ|r_k|) confirms diminishing returns beyond a small k, which is important for DSS interpretability. Robustness checks using temporal blocks and bootstrap confidence intervals indicate stable correlation signs across blocks and bootstrap distributions whose intervals do not cross zero.

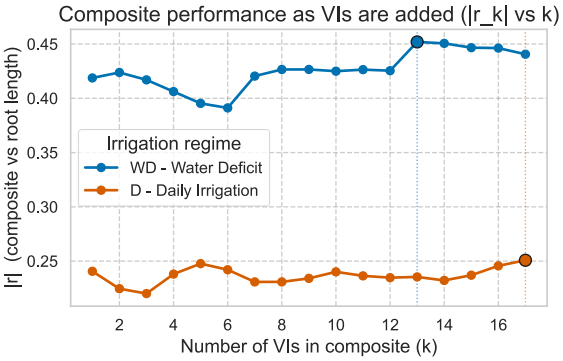

Figure 40. Correlation trajectories for greedy composite VI construction (|r_k| vs k) under WD and D. Curves showing how composite–root correlations change as additional VIs are added. The strongest improvements occur at k = 1–3, after which gains plateau or decline, demonstrating diminishing returns and supporting low-dimensional composite design

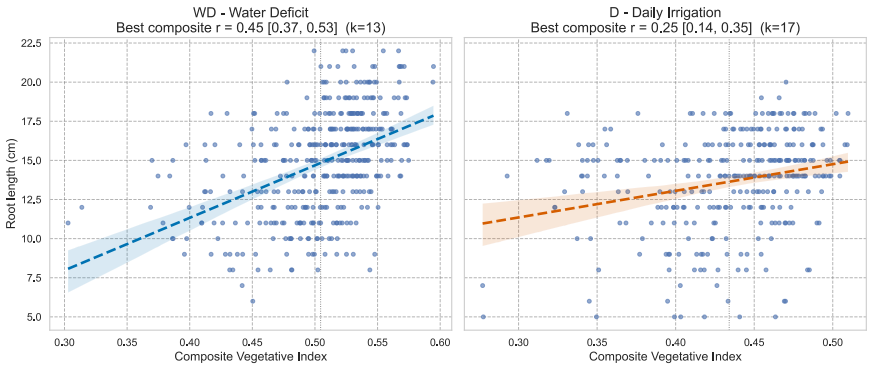

Figure 41. Scatterplots of root length versus the best composite VI for each irrigation regime. Plots showing that composite indices achieve equal or slightly stronger correlations than the best single VI, with stable regression lines and Fisher-transformed confidence intervals excluding zero. Composites smooth noise and better represent integrated canopy signals.

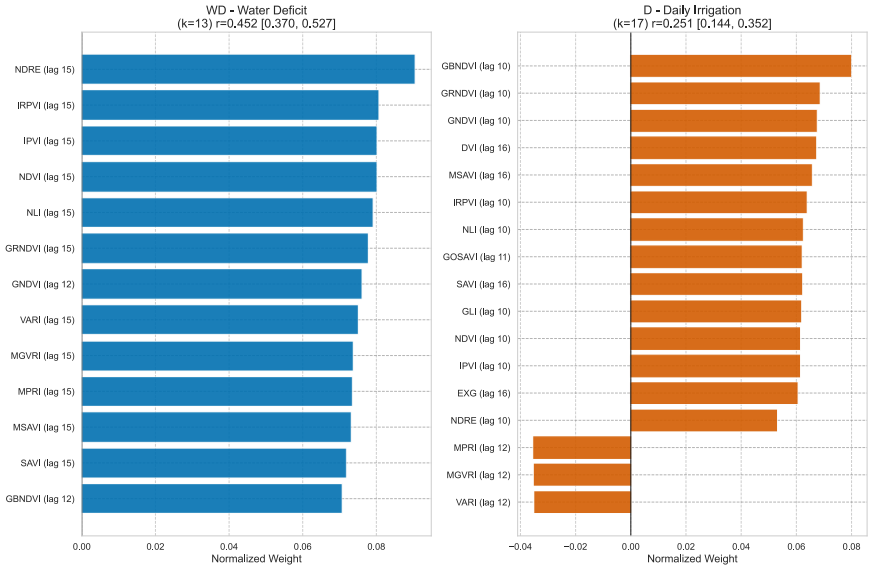

Figure 42. Normalised VI weight profiles for the best composite index under each irrigation regime. Weight distributions showing that only a few VIs carry strong influence in each composite, while most contribute marginally. High-weight VIs correspond to those with strong individual correlations, indicating internal consistency in composite construction.

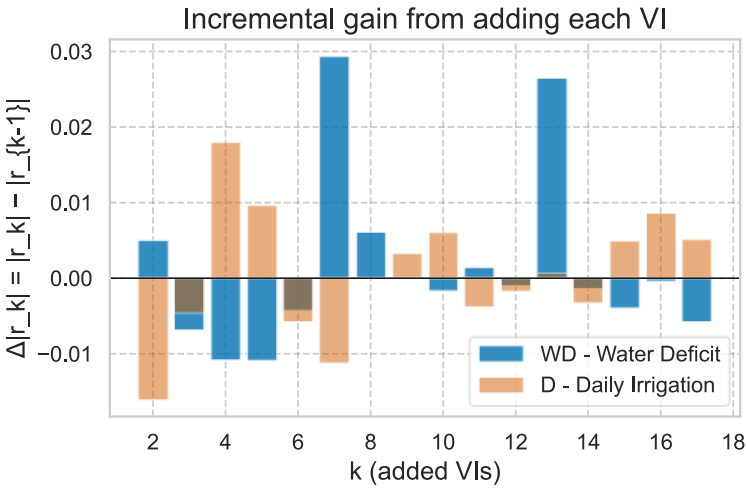

Figure 43. Change in composite–root correlation (Δ|r_k|) as a function of composite size (k). Δ|r_k| plots illustrating that the largest improvements occur when moving from k = 1 to k = 2–3. Later additions yield negligible or negative changes, reinforcing the optimality of small composites for DSS use.

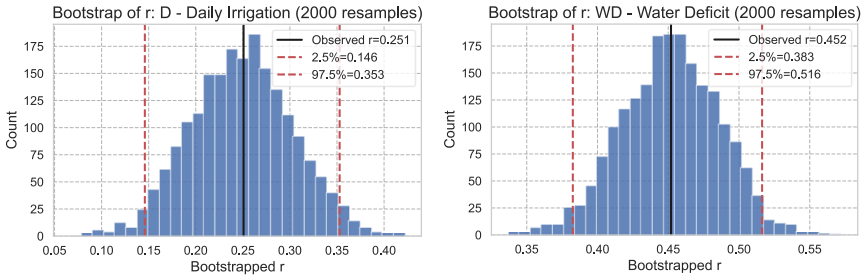

Figure 44 and Figure 45. Robustness checks for composite–root relationships: temporal block correlations and bootstrap confidence intervals. Panels showing stable correlation signs across temporal blocks and unimodal bootstrap distributions with 95% intervals not crossing zero. These results confirm that composite–root linkages are seasonally persistent and not driven by isolated events.

6) Predictive modelling of root length (ENV vs ENV+VI/CVI; regime-specific)

Across regimes, predictive models explain a moderate share of variance on test sets. For **Daily (D)**, the best configuration is **Linear regression with ENV + single best VI (FeatureSet B)** with **$R^2 \approx 0.47$** and **RMSE ≈ 2.04 cm**, while ENV-only models are weaker (**$R^2 \approx 0.25$**). For **Water deficit (WD)**, the best is **Random Forest with ENV + single VI (FeatureSet B)** with

$R^2 \approx 0.43$ and **RMSE ≈ 2.74 cm**, while ENV-only models already perform strongly (**$R^2 \approx 0.42$**). Adding both single VI and CVI together does not produce consistent gains, implying redundancy. Inter-annual transfer tests (train 2023 → test 2024) return negative R^2 values, indicating that year-specific recalibration is needed for operational use.

Table 12. Predictive model performance for root-length forecasting under daily (D) and water-deficit (WD) irrigation. Test-set R^2 and RMSE for four learners (Linear, Gradient Boosting, LightGBM, Random Forest) using different feature sets (ENV only; ENV + single VI; ENV + CVI; ENV + both). ENV+single VI provides the most reliable gains, particularly under daily irrigation. Inter-year transfer models (2023→2024) perform poorly, confirming the need for annual recalibration.

Regime	Model	FeatureSet	R2	RMSE
D - Daily Irrigation	GBM_2023→2024	A_ENV	-2.97	NaN
	GradientBoosting	C_ENV+CVI	0.467	2.26
	LightGBM	C_ENV+CVI	0.456	2.28
	Linear	B_ENV+SINGLE	0.472	2.04
	RandomForest	C_ENV+CVI	0.419	2.36
WD - Water Deficit	GBM_2023→2024	B_ENV+SINGLE	-1.182	NaN
	GradientBoosting	A_ENV	0.423	2.31
	LightGBM	A_ENV	0.423	2.31
	Linear	D_ENV+SINGLE+CVI	0.403	2.81
	RandomForest	B_ENV+SINGLE	0.431	2.74

SHAP summaries for ENV+CVI models show that environmental drivers (moisture availability and atmospheric demand variables) dominate contributions in both regimes, with the composite VI acting as a secondary, physiologically consistent canopy state modifier.

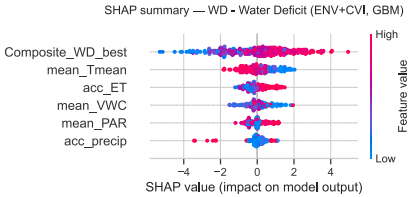

Figure 46. SHAP summary — D (ENV+CVI, GBM). *Features ranked by mean absolute SHAP value for a gradient-boosting model fit within the D regime using environmental covariates plus the best CVI. Points show per-sample SHAP contributions; color encodes feature value (blue = low, pink = high).*

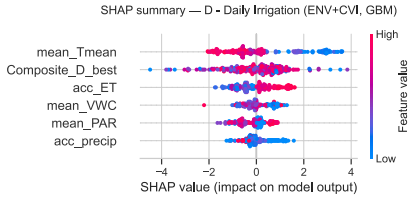

Figure 47. SHAP summary — WD (ENV+CVI, GBM). Composite_WD_best *has the largest and most consistently positive impact, followed by air temperature and cumulative ET, underscoring the predictive value of multispectral information under deficit irrigation.*

Part 3 provides two complementary root signals for the DSS: (i) a seasonal, stress-sensitive trajectory where WD consistently stabilizes root length during heat-wave windows, and (ii) an operational proxy layer where a small number of lagged VIs, preferably as a low-dimensional composite, can track and modestly improve forecasts of root length when paired with environmental drivers. Together, these outputs support discretised BN states for "root condition" and allow root depth to act as a medium-term constraint on both irrigation threshold selection and nitrogen safety margins under sand-based conditions.

The root results show that irrigation strategy shapes a predictable seasonal rooting envelope and that canopy spectral signals can serve as a compact proxy for belowground status when aligned with appropriate lags. This sets up Part 4, where the remote sensing component is expanded beyond root proxies to broader canopy monitoring, spatial AOI heterogeneity, and the extraction of vegetation indices that can continuously update stress and performance states across the entire green surface.

3.4 Part 4. Vegetative indices analysis and remote sensing pipeline

Parts 1–3 established that (i) nitrogen dynamics and clipping-based demand signals are constrained by short stress windows, (ii) irrigation thresholds are governed by ETc-driven depletion and spatial heterogeneity, and (iii) root condition responds predictably to irrigation regime and can be proxied by lagged VIs. Part 4 extends this by building a defensible remote-sensing pipeline: first ensuring that VI statistics represent turf-only AOIs, then compressing multi-season VI archives into stable canopy regimes and VI families that can be simplified into BN/DSS input nodes.

1) U-Net segmentation of putting greens (computer-vision front end)

Motivation and model shift. A reliable AOI definition is a prerequisite for meaningful VI time series. Patch-based CNN classification (green vs non-green) produced ragged edges and misclassified collars under illumination gradients and partial shade. A **U-Net semantic segmentation model** was therefore implemented to generate full-image, pixel-wise masks with geometric continuity suitable for downstream VI extraction.

Training data and setup. UAV RGB frames (native **2560×1440**) were extracted and manually annotated to label putting-green boundaries. Frames were pooled across multiple labeling "jobs" and split **70/15/15** into train/val/test per job. Images were resized to **512×512**, augmented (rotation, scaling, flips), and normalised (ImageNet statistics). The U-Net used RGB input and one output class (green), with encoder–decoder structure (64/128 down-sampling stages, 256 bottleneck), Adam (LR $\mathbf{1\times10^{-4}}$), BCEWithLogits loss, StepLR scheduler, batch size **12**, evaluated using **IoU** and **Dice** per epoch.

Training performance. Loss decreased rapidly within ~20–30 epochs and remained low (<0.02) through training. Validation loss declined from ~0.25–0.30 initially to ~0.001–0.005 in final epochs. Median validation performance was high (**IoU ~0.95**, **Dice ~0.96**), with late

epochs approaching **IoU ≈ 0.99** and **Dice ≈ 0.99**. Training–validation loss closely tracked, indicating limited overfitting.

Qualitative mask fidelity and implications. Predicted masks captured full green geometry (curved perimeters, lobes), excluding bunkers, collars, paths, and rough even when colour/texture differences were subtle. Full-resolution masks preserved the original grid, enabling direct reuse for UAV and PlanetScope VI extraction and supporting within-green heatmaps and percentile/CV statistics. In the DSS, segmentation quality directly affects VI node calibration and therefore the trustworthiness of inferred stress, N status, and moisture-state evidence.

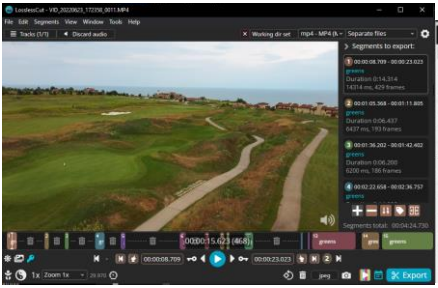

Figure 48. Example of UAV frame extraction for segmentation training

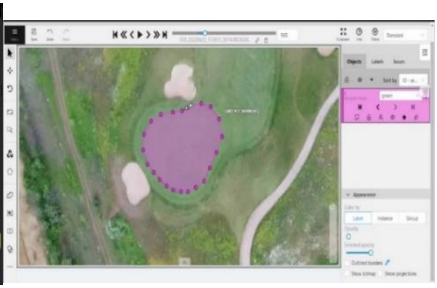

Figure 49. Manual annotation of putting-green boundaries for U-Net training.

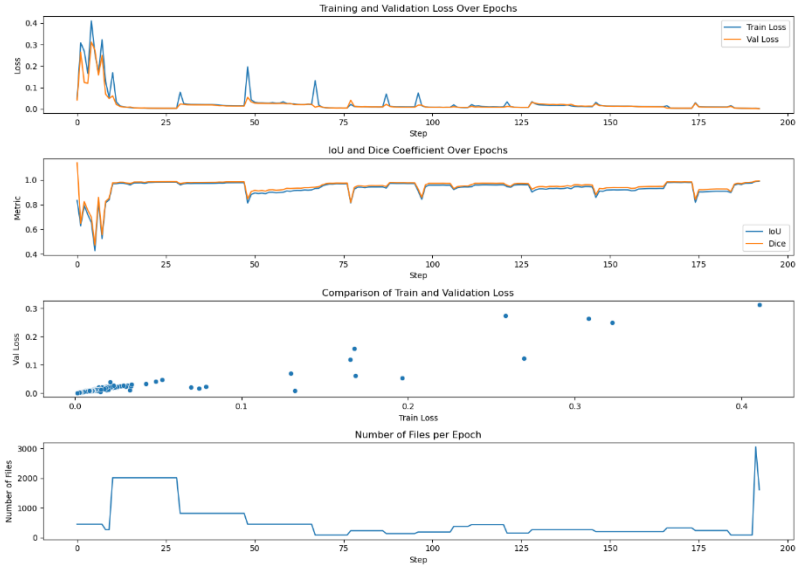

Figure 50. Training and validation performance of the U-Net segmentation model. Loss curves, IoU and Dice trajectories, and per-epoch dataset size illustrate rapid convergence within the first 20–30

epochs and stable generalisation thereafter. Final validation IoU and Dice values approach 0.99, indicating high-fidelity segmentation of putting-green surfaces.

Figure 51. Predicted segmentation masks on held-out UAV frames. An example demonstrating the U-Net's ability to capture curved perimeters, narrow collars, and subtle geometric features while excluding bunkers, paths, and rough. High-resolution masks (2560×1440) support downstream VI extraction without resizing artefacts

2) Multi-season canopy regimes via temporal-feature clustering (k = 10)

Approach. The multi-season archive was compressed by computing, per pixel and per VI, three temporal descriptors (**mean, variance, trend**), then clustering pixels into **k = 10** regimes. Cluster IDs were relabelled by increasing mean value to create an intuitive ordering from chronically weak/bare surfaces to persistently dense high-VI canopy.

Full-course results (GCA, GCB). NDVI and NDRE clustering produced consistent spatial structure: low-mean clusters (0–3) were mainly non-turf (trees/buildings/peripheral roughs) and areas affected by cloud contamination. Intermediate clusters (4–6) aligned with fairway corridors and semi-managed rough, showing moderate VI and higher variance. High-mean clusters (7–9) aligned with segmented putting greens and a limited number of intensively irrigated surrounds, characterised by high mean VI and relatively low variance. Similar ordering emerged across indices, indicating the regimes reflect persistent turf–non-turf mosaics rather than index artefacts.

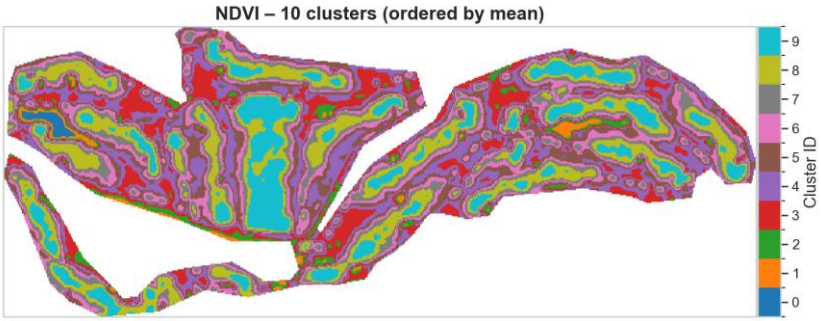

Figure 52. Example of multi-season NDVI clustering results (k = 10) across the full GCA

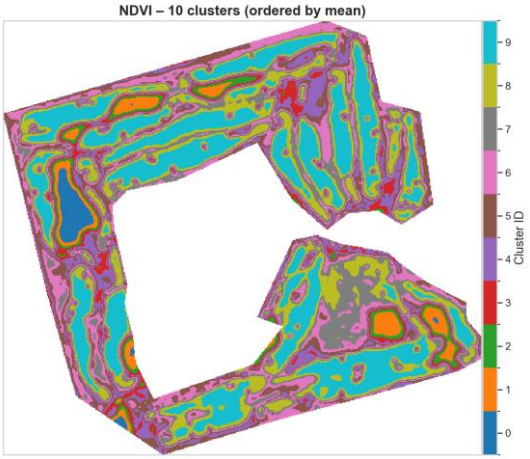

Figure 53. Example of multi-season NDVI clustering results (k = 10) across the full GCB.

3) Greens vs fairways in regime space (cluster overlap/composition)

Intersecting cluster maps with binary masks for **greens** and **fairways** quantified how each surface occupies canopy regime space. Fairways spread across intermediate and high clusters, reflecting heterogeneity from partial irrigation, mowing variation, slopes, and episodic stress. Greens were dominated by the highest regimes, with more than half of green area in the top cluster (ID 9), and the remainder primarily in cluster 8, consistent with dense, stable canopies. VI limitations were visible: **NDVI showed saturation** (strong concentration in highest clusters), whereas **MPRI preserved broader variability** across clusters even on greens. The same qualitative separation (greens concentrated in top regimes; fairways distributed across intermediate regimes) was observed across both GCA and GCB.

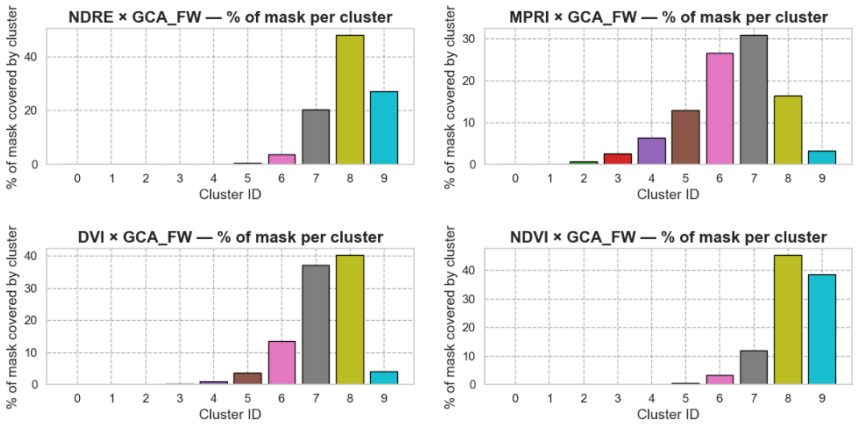

Figure 54 . Cluster-composition of fairway pixels: example distribution for NDRE, MPRI, DVI, NDVI (GCA).

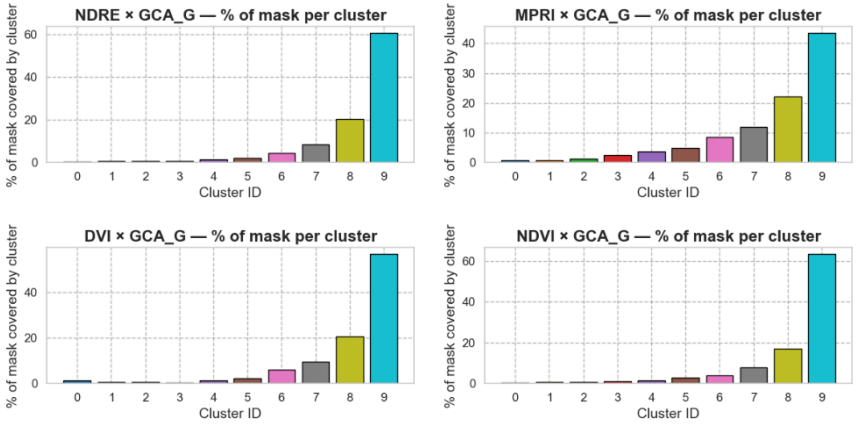

Figure 55. Cluster-composition of putting-green pixels: example distribution for NDRE, MPRI, DVI, NDVI (GCA).

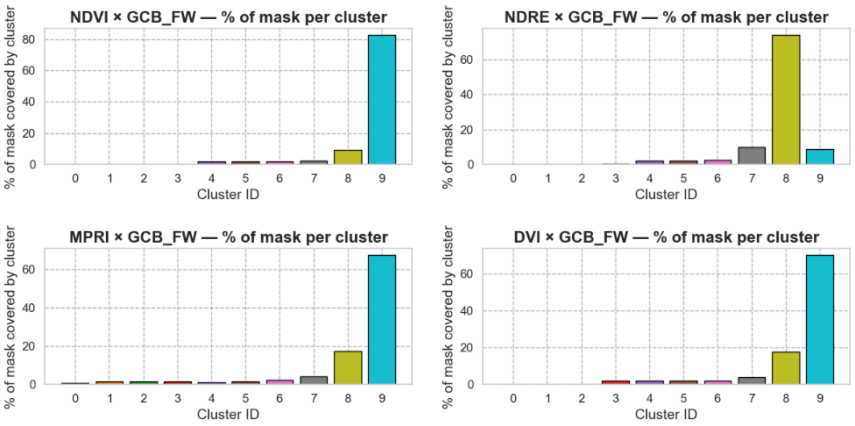

Figure 56. Cluster-composition of fairway pixels: examples for NDRE, MPRI, DVI, NDVI (GCB)

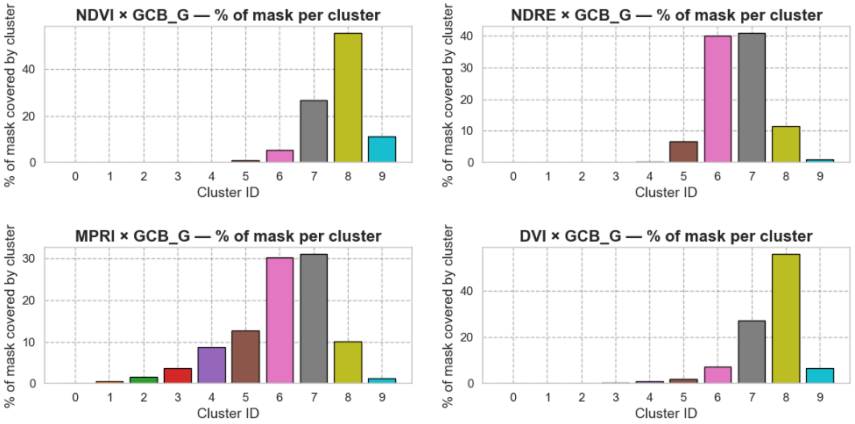

Figure 57. Cluster-composition of putting-green pixels: examples for NDRE, MPRI, DVI, NDVI (GCB).

4) Similarity families of VIs (per surface and per site)

Because many indices convey overlapping information, similarity-family analysis grouped VIs with shared multi-season behaviour separately for **fairways (FW)** and **greens (G)**.

GCA fairways (Table 30; Figure 78). Families included: (i) visible-band contrast plus soil-adjusted NIR (DVI/GLI/MSAVI/SAVI), (ii) colour-stress indices (EXG/MGVRI/MPRI/VARI), (iii) green–NIR structural pair (GBNDVI/GNDVI), (iv) standalone MSR, (v) standalone RVI, (vi) high-density structural ensemble (GRNDVI/IPVI/IRPVI/NDVI), and (vii) red-edge/soil-adjusted hybrids (GOSAVI/NDRE/NLI).

*Table 13. GCA Fairways **similarity groups**, Similarity families obtained from multi-season clustering of VI trajectories across fairways. Each group represents a set of indices with shared temporal behaviour and physiological meaning (colour-based stress, structural NIR–green ensembles, red-edge variants).*

GCA Fairways Similarity groups		
Group	**VI**	
Group 0 Visible-band contrast with soil-adjusted NIR VIs	DVI, GLI, MSAVI, SAVI	This group blends simple visible-band contrast indices (DVI, GLI) with soil-adjusted NIR formulations (MSAVI, SAVI). Their shared overlap pattern suggests that under fairway conditions, soil brightness, partial canopy cover, and moderate biomass levels create conditions where visible-band contrast and soil-adjusted NIR ratios respond similarly.
Group 1 Colour-contrast indices	EXG, MGVRI, MPRI, VARI	These indices cluster together because they emphasise short-term colour changes linked to heat, drought, mowing patterns, and surface quality. Their grouping confirms that colour-space transformations (EXG, VARI) and green–red gradients (MGVRI, MPRI) encode a shared stress-sensitive signal.
Group 2 Green–NIR two-band structural VIs	GBNDVI, GNDVI	These indices form a compact family capturing NIR–green structure in medium-density canopies. Their behaviour remains distinct from NDVI or red-edge formulations, indicating unique sensitivity to moderate canopy thinning.
Group 3	MSR	The Modified Simple Ratio forms a unique group. Its normalisation of RVI and reduced sensitivity to illumination produces a signature that does not align with any other family on fairways.
Group 4 Ratios	RVI	This index stands alone, reflecting its tendency to saturate more quickly and produce behaviour distinct from difference-based indices.
Group 5 High-density NIR-green/red families	GRNDVI, IPVI, IRPVI, NDVI	These indices cluster into a shared structural family representing stable chlorophyll-related behaviour. They capture the higher-end of canopy reflectance dynamics and share nearly identical spatial signatures.
Group 6 Red-edge and soil-adjusted hybrids	GOSAVI, NDRE, NLI	These indices express the red-edge and soil-adjusted behaviour under fairway heterogeneity. Their grouping indicates sensitivity to intermediate canopy density and subtle biochemical variation.

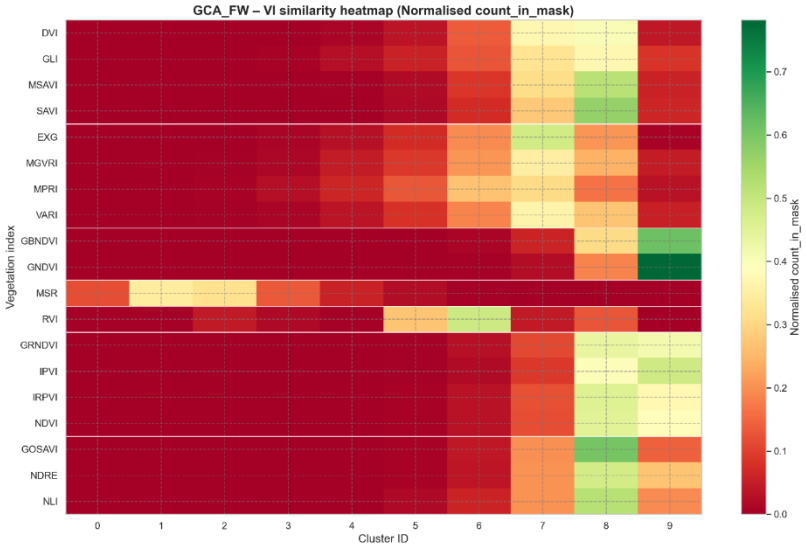

Figure 58. Visualisation of VI similarity groups for GCA fairways

GCA greens (Table 31; Figure 79). Greens showed greater differentiation despite canopy uniformity: (i) colour/brightness family (EXG/GLI/MGVRI/VARI), (ii) broad structural NIR family (GBNDVI/GOSAVI/GRNDVI/IRPVI/NDVI/NLI), (iii) soil-adjusted + red-edge family (DVI/MSAVI/NDRE/SAVI), with RVI/MSR remaining isolated and MPRI forming an independent cluster.

Table 14. GCA G Similarity groups. Similarity groupings of multi-season VI behaviour on putting greens. Structural NIR–red/green families dominate, while colour-based VIs form a distinct group capturing subtle brightness and hue shifts on dense turf.

GCA G Similarity groups		
Group	VI	
Group 0 Surface colour and brightness	EXG, GLI, MGVRI, VARI	These indices isolate rapidly changing colour and brightness patterns on greens. Their grouping shows that despite canopy uniformity, subtle surface colour variations remain detectable at pixel scale
Group 1 Structural NIR/green–red	GBNDVI, GOSAVI, GRNDVI, IRPVI, NDVI, NLI	This broad family represents the dominant structural signal of dense turf. Here, NDVI merges with G*NDVI-type indices and soil-adjusted variants (GOSAVI, NLI), indicating that under high canopy density, multiple NIR-based formulations converge to the same spectral behaviour.
Group 2 Soil-adjusted and red-edge VIs	DVI, MSAVI, NDRE, SAVI	Unlike fairways, these indices form a separate group. The presence of NDRE shows that even on greens, slight biochemical variation persists, while MSAVI and SAVI map small changes in canopy thickness. DVI joins this group because visible-band

		differences become structurally similar when the canopy is uniformly dense.
Group 3	RVI	Still behaves independently because ratio-based indices saturate strongly on greens and lose contrast relative to difference-based indices.
Group 4 NIR-green structural	GNDVI, IPVI	This group captures the most stable portion of the high-density canopy signal. Their convergence suggests consistency in how green–NIR ratios behave across multi-season imagery.
Group 5	MSR	Again isolated as a standalone group, consistent with fairway behaviour.
Group 6	MPRI	Forms its own cluster, indicating that on greens it captures a colour variation distinct from the broader stress-colour family.

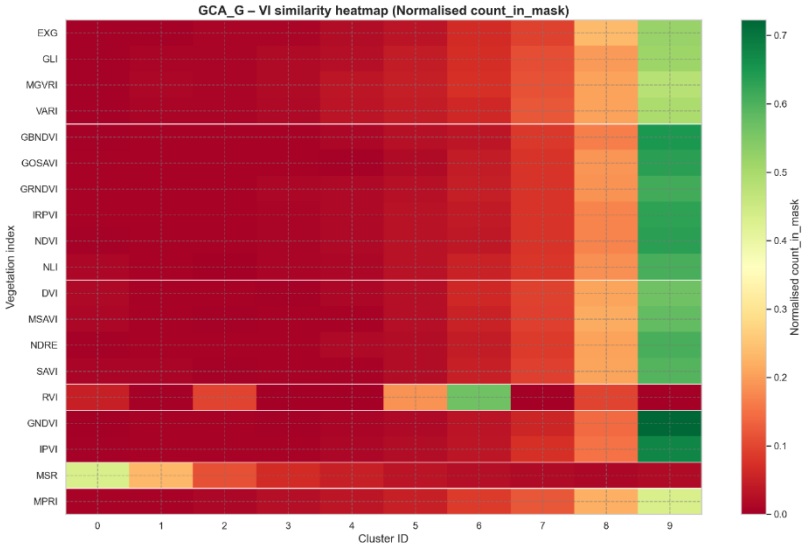

Figure 59. Visualisation of VI similarity groups for GCA greens

GCB fairways and greens (Tables 32–33; Figures 80–81). The overall structure resembled GCA, but several shifts suggest stronger separation between colour indices and structural indices, and more site-specific red-edge behaviour. On GCB fairways, VARI separated as its own family, and **NDRE formed its own group** rather than merging with soil-adjusted/red-edge hybrids. On GCB greens, a mixed family formed between colour indices and NDRE, while the structural ensemble remained dominant; EXG separated independently.

Across both courses, these patterns support a physically grounded simplification: **structural NIR-based indices** form the backbone of canopy density information, **colour indices** capture short-term stress/brightness shifts, **soil-adjusted indices** behave differently depending on

canopy density and soil exposure, and **red-edge indices** may either merge with structural signals or separate depending on site-specific biochemical gradients.

Table 15. GCB fairways VI similarity groups. Similarity families for GCB fairways. The grouping shows stronger separation between colour-based indices and structural ensemble VIs compared with GCA, with site-specific behaviour for VARI and NDRE.

GCB Similarity groups		
Group	**VI**	
Group 0 Visible-band contrast + soil-adjusted indices	DVI, MPRI, MSAVI, SAVI	This group merges simple visible-index differences (DVI, MPRI) with soil-adjusted NIR indices (MSAVI, SAVI). Their overlap pattern suggests that fairway canopy density at GCB often exposes soil background (**regular hollow tine aeration**), causing these indices to respond similarly.
Group 1 High-density structural NIR/green/red ensemble	GBNDVI, GNDVI, GOSAVI, GRNDVI, IPVI, IRPVI, NDVI, NLI	This large family represents the structural canopy signal across fairways. These VIs converge where the canopy is moderately stable, irrigated, and biochemical variation is low. Their grouping matches what was observed at GCA, but with stronger consolidation, indicating reduced separation between green- and red-edge-driven formulations.
Group 2 Colour-based stress/brightness indices	EXG, GLI, MGVRI	This group captures rapid colour or spectral brightness changes associated with mowing, traffic, partial drought, or shallow soil moisture variability. The separation from Family 3 (VARI alone) suggests GLI and EXG behave differently at GCB than at GCA, likely due to different mowing height (**FW is creeping bentgrass, maintained at lower height**) and soil type (**FW is sand, compared to top soil for GCA**).
Group 3	VARI	VARI isolates into its own group, reflecting its strong sensitivity to green/red/blue balance under uneven illumination. On GCB fairways, VARI identifies stress signatures not fully captured by the EXG-GLI cluster.
Group 4	RVI	As in GCA, RVI saturates quickly and remains isolated.
Group 5	MSR	Non-linear scaling causes MSR to behave uniquely, separating from the red-edge and NIR families.
Group 6	NDRE	Unlike GCA where NDRE grouped with soil-adjusted indices, it forms its own family at GCB. This indicates unique behaviour of the red-edge on these fairways, possibly due to stronger spatial heterogeneity, surface maintenance or red-edge sensitivity to subtle canopy stress.

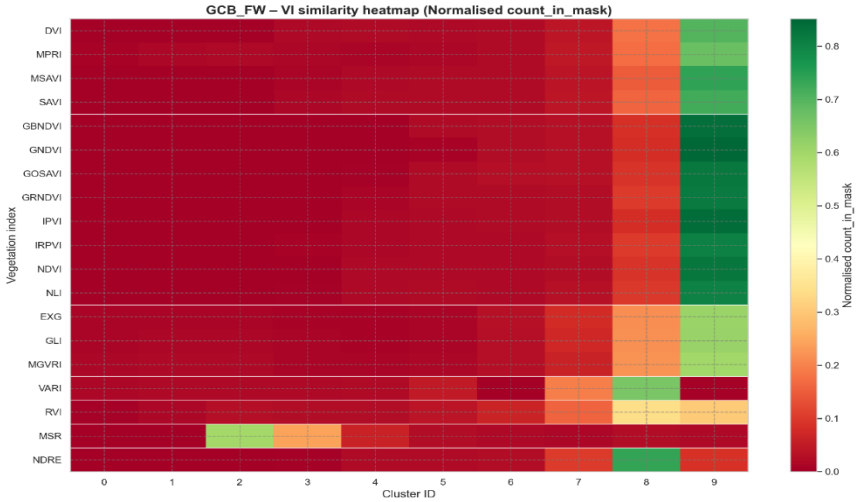

Figure 60. Visualisation of VI similarity groups for GCB fairways.

Table 16. GCB greens VI similarity groups. Grouping results for putting greens at GCB, with colour-based indices and NDRE forming a mixed family, and structural NIR–red/green indices forming the dominant ensemble. MSR and RVI remain isolated due to saturation properties.

GCB- G Similarity groups		
Group	VI	
Group 0 Colour-space and partial red-edge	GLI, MGVRI, MPRI, NDRE	A unique mixture of colour-based indices. On dense greens, NDRE often collapses into the structural family, but here it aligns with colour indices, likely reflecting slight biochemical variations correlated with colour variability.
Group 1 Broad structural NIR–red/green	DVI, GRNDVI, IRPVI, MSAVI, NDVI, NLI, SAVI	This large family captures the core structural signature of dense greens, where soil-adjusted indices and NIR–green/red ratios converge. This matches GCA, but with GRNDVI and DVI added, showing stronger convergence across canopy thickness gradients.
Group 2 Green–NIR subset	GBNDVI, GNDVI, GOSAVI, IPVI	A stable NIR–green subset reflecting consistent structural behaviour under irrigated high-density greens
Group 3	RVI	Again isolated because of saturation effects
Group 4	VARI	VARI maintains independence, capturing colour behaviour distinct from structural indices.
Group 5	MSR	Behaves as a unique non-linear formulation
Group 6	EXG	Separates from other colour indices at GCB, reflecting distinctive contrast behaviour on these greens (likely influenced by mowing patterns and localised colour variation).

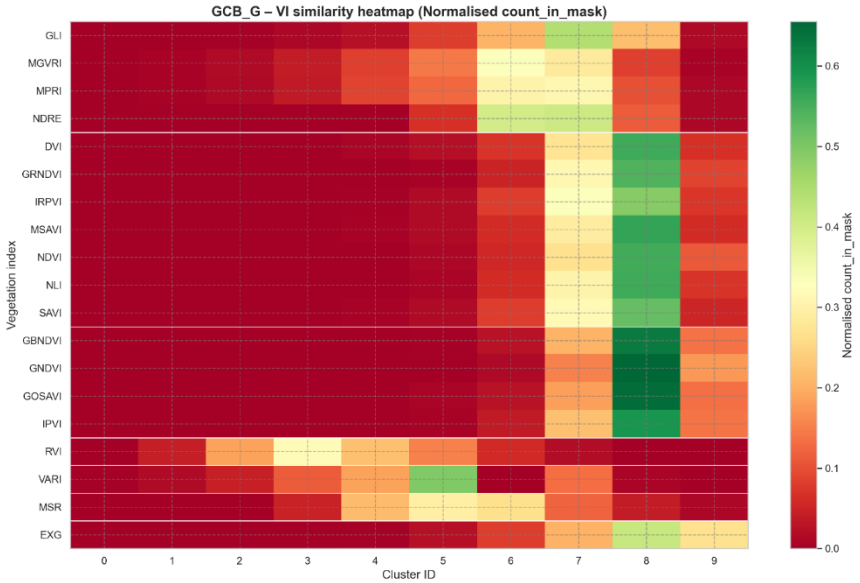

Figure 61. Visualisation of VI similarity groups for GCB greens

5) Daily sensitivity and predictive performance within VI families (selection of representatives)

Daily interpolated VIs were merged with daily weather variables (Tmax, Tmin, ET0, VPD, rainfall, wind, etc.) and evaluated using: (i) best Pearson correlation, (ii) best Spearman correlation, and (iii) Random Forest multivariate performance metrics. The results were consistent across surfaces and sites:

- **Structural indices** (NDVI/GNDVI) showed the highest explanatory power and stable behaviour across clubs and surfaces.
- **Colour-stress indices** (MGVRI and VARI) were most responsive to rapid stress and mowing-related colour shifts.
- **Soil-adjusted indices** (MSAVI) provided strongest performance under partial soil exposure, especially on fairways.
- **Red-edge (NDRE)** showed variable behaviour but stronger explanatory power where biochemical gradients were more pronounced (notably at GCB).
- **Non-linear/saturated indices** (MSR, RVI) showed limited added value and lower interpretability.

These results supported selecting one representative VI per family for DSS integration.

Table 17. Daily sensitivity and predictive performance of VIs (GCA fairways). Summary of Pearson/Spearman correlations, optimal lags, and Random Forest performance metrics for each VI. Structural indices (NDVI, GOSAVI) and soil-adjusted indices (MSAVI) show highest explanatory power, while visible-range colour indices respond primarily to stress and mowing patterns

Daily sensitivity and predictive performance GCA FW							
VI	Best_Pearson	**Best_Spearman**	**Best_Lag**	**Lag_Corr**	**RF_R2**	**RF_RMSE**	**Group**
DVI	0.651	0.562	0	0.651	0.943	0.013	0
MSAVI	0.649	0.521	0	0.649	0.945	0.020	0
GLI	0.190	0.156	6	0.213	0.898	0.019	0
SAVI	0.630	0.504	0	0.630	0.941	0.017	0
MGVRI	0.227	0.242	3	0.236	0.908	0.038	1
EXG	0.436	0.341	2	0.442	0.923	0.001	1
MPRI	0.226	0.243	3	0.236	0.908	0.020	1
VARI	0.226	0.244	3	0.235	0.908	0.026	1
GBNDVI	0.234	0.204	1	0.241	0.882	0.019	2
GNDVI	0.229	0.208	6	0.237	0.879	0.011	2
MSR	0.219	0.176	6	0.245	0.894	0.004	3
RVI	0.185	0.161	6	0.212	0.896	0.726	4
GRNDVI	0.239	0.196	6	0.257	0.885	0.022	5
IPVI	0.238	0.183	6	0.261	0.890	0.008	5
IRPVI	0.235	0.182	6	0.259	0.889	0.015	5
NDVI	0.238	0.183	6	0.261	0.889	0.017	5
GOSAVI	0.593	0.492	0	0.593	0.931	0.014	6
NDRE	0.339	0.383	14	0.399	0.897	0.014	6
NLI	0.368	0.344	3	0.375	0.907	0.055	6

Table 18. Daily sensitivity and predictive performance of VIs (GCA greens). Performance metrics for each VI on dense green canopies. DVI, MSAVI and SAVI rank highest in structural sensitivity; NDRE captures red-edge biochemical variation; colour indices show weaker but complementary signals.

Daily sensitivity and predictive performance GCA G							
VI	**Best_Pearson**	**Best_Spearman**	**Best_Lag**	**Lag_Corr**	**RF_R2**	**RF_RMSE**	**Group**
EXG	0.416	0.354	1	0.421	0.916	0.002	0
GLI	0.213	0.194	6	0.242	0.891	0.020	0
MGVRI	0.188	0.167	12	0.235	0.896	0.042	0
VARI	0.186	0.163	12	0.232	0.896	0.029	0
GBNDVI	0.250	0.219	14	0.258	0.877	0.019	1
GOSAVI	0.559	0.477	0	0.559	0.928	0.014	1
GRNDVI	0.264	0.217	5	0.292	0.881	0.021	1
IRPVI	0.256	0.208	14	0.288	0.884	0.014	1
NDVI	0.259	0.210	14	0.288	0.885	0.016	1
NLI	0.337	0.357	1	0.341	0.902	0.054	1
DVI	0.631	0.533	0	0.631	0.941	0.014	2
MSAVI	0.624	0.497	0	0.624	0.942	0.021	2
NDRE	0.399	0.491	14	0.478	0.903	0.014	2
SAVI	0.602	0.484	0	0.602	0.937	0.018	2
RVI	0.228	0.195	7	0.276	0.888	0.721	3
IPVI	0.259	0.210	14	0.288	0.885	0.008	4
GNDVI	0.269	0.251	11	0.280	0.878	0.011	4
MSR	0.244	0.203	7	0.283	0.887	0.004	5
MPRI	0.188	0.167	12	0.235	0.896	0.021	6

Table 19. Daily sensitivity and predictive performance of VIs (GCB fairways). Performance summary showing strong predictive power of MPRI, MGVRI, EXG and NLI for stress-related responses, and GNDVI/IPVI/NDVI for structural behaviour. NDRE shows strong lagged correlation at GCB.

Daily sensitivity and predictive performance GCB FW							
VI	**Best_Pearson**	**Best_Spearman**	**Best_Lag**	**Lag_Corr**	**RF_R2**	**RF_RMSE**	**Group**
DVI	0.374	0.345	11	0.389	0.900	0.032	0
MPRI	0.654	0.641	14	0.775	0.956	0.021	0
MSAVI	0.410	0.401	14	0.481	0.912	0.037	0
SAVI	0.439	0.428	14	0.517	0.919	0.030	0
GBNDVI	0.244	0.323	14	0.285	0.900	0.068	1
GNDVI	0.276	0.329	14	0.314	0.905	0.039	1
GOSAVI	0.362	0.308	14	0.474	0.934	0.015	1
GRNDVI	0.372	0.395	14	0.479	0.921	0.052	1
IPVI	0.482	0.482	14	0.594	0.943	0.016	1
IRPVI	0.477	0.479	14	0.591	0.942	0.026	1
NDVI	0.482	0.482	14	0.594	0.943	0.032	1
NLI	0.544	0.540	14	0.706	0.954	0.047	1
EXG	0.622	0.572	14	0.691	0.947	0.004	2
GLI	0.468	0.490	14	0.575	0.928	0.021	2
MGVRI	0.655	0.641	14	0.776	0.957	0.040	2
VARI	0.583	0.577	14	0.677	0.936	0.060	3
RVI	0.372	0.456	3	0.404	0.912	1.240	4
MSR	0.375	0.421	8	0.406	0.915	0.006	5
NDRE	0.508	0.536	14	0.583	0.937	0.030	6

Table 20. Daily sensitivity and predictive performance of VIs (GCB greens). Metrics showing that colour-stress indices (GLI, MGVRI, MPRI) outperform structural indices in explaining variability on dense greens at GCB, reflecting local sensitivity to subtle colour shifts and stress gradients.

Daily sensitivity and predictive performance GCB G							
VI	**Best_Pearson**	**Best_Spearman**	**Best_Lag**	**Lag_Corr**	**RF_R2**	**RF_RMSE**	**Group**
GLI	0.587	0.606	14	0.653	0.937	0.017	0
MGVRI	0.698	0.693	14	0.761	0.947	0.039	0
MPRI	0.697	0.694	14	0.761	0.947	0.020	0
NDRE	0.546	0.560	14	0.592	0.934	0.028	0
DVI	0.487	0.431	0	0.487	0.906	0.029	1
GRNDVI	0.424	0.444	14	0.500	0.918	0.049	1
IRPVI	0.548	0.546	14	0.626	0.940	0.024	1
MSAVI	0.552	0.530	11	0.569	0.917	0.033	1
NDVI	0.552	0.547	14	0.630	0.941	0.029	1
NLI	0.720	0.708	14	0.801	0.959	0.043	1
SAVI	0.581	0.563	12	0.604	0.924	0.027	1
GBNDVI	0.268	0.356	14	0.336	0.899	0.067	2
GNDVI	0.306	0.362	14	0.377	0.903	0.038	2
GOSAVI	0.565	0.493	14	0.663	0.942	0.013	2
IPVI	0.552	0.547	14	0.630	0.941	0.015	2
RVI	0.467	0.537	14	0.539	0.919	0.845	3
VARI	0.614	0.615	14	0.669	0.930	0.052	4
MSR	0.447	0.515	14	0.476	0.916	0.005	5
EXG	0.710	0.692	11	0.746	0.948	0.004	6

Table 21. Representative VI selection for DSS integration based on family behaviour, sensitivity and predictive accuracy. Representative indices (NDVI/GNDVI, MGVRI/VARI, MSAVI, NDRE) summarise distinct physiological components—structural density, colour-stress response, soil adjustment, and red-edge biochemical sensitivity—ensuring interpretable and non-redundant BN nodes.

Family	Representative VI	Rationale
Structural indices	NDVI or GNDVI	Highest RF_R2, stable across clubs and surfaces, interpretable canopy-thickness signal
Colour-based stress	MGVRI or VARI	Strong response to heat/drought stress events; VARI independent at both clubs
Soil-adjusted	MSAVI	Best performance across fairways and greens; robust under partial soil exposure
Red-edge	NDRE	Useful for biochemical stress detection; site-specific value at 27Club
Nonlinear/saturated families	Excluded	Limited added value, low interpretability

6) DSS-oriented condensation: BN input nodes derived from VI families

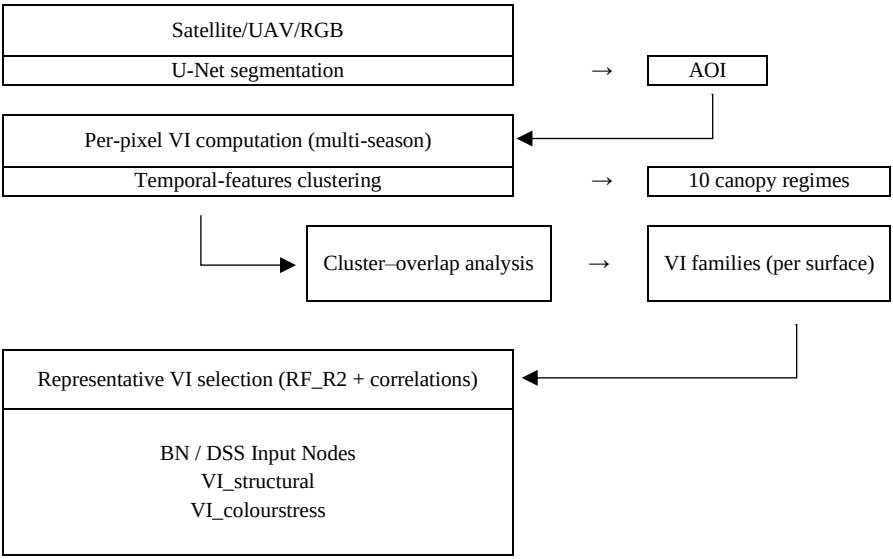

Figure 62. Schematic workflow of the Remote Sensing chapter and DSS integration. Process diagram connecting UAV/satellite imagery, U-Net segmentation, pixel-wise VI extraction, temporal-features clustering, VI family formation, representative VI selection, and downstream BN/DSS node construction (VI_structural, VI_colourstress, VI_soiladjusted, VI_rededge).

To reduce redundancy and maintain interpretability, the DSS uses VI-family representatives as BN evidence nodes rather than many raw indices. The proposed mapping is:

- **VI_structural:** NDVI or GNDVI
- VI_colourstress: MGVRI or VARI
- VI_soiladjusted: MSAVI
- **VI_rededge:** NDRE (optional; depending on BN complexity and site relevance)

These nodes feed different DSS modules: Nitrogen (structural + colour-stress), Irrigation (structural + colour-stress + soil-adjusted), Root development (lagged structural + colour-stress), and global causal nodes such as canopy_density_state, stress_state, and water_deficit_state.

Part 4 establishes a complete and defensible remote-sensing layer: segmentation guarantees turf-only AOIs, multi-season clustering compresses the archive into repeatable canopy regimes, and similarity families reduce the VI space into interpretable representatives. This output is the necessary bridge to Part 5, where these VI nodes become observable evidence

within the Bayesian Network and are combined with nitrogen, irrigation, and root modules to produce probabilistic state inference and management recommendations under uncertainty.

3.5 Part 5. AI-Based Bayesian Decision-Support System (BN-DSS)

Parts 1–4 generated separate, evidence-rich components (nitrogen and SOM dynamics, irrigation thresholds and spatial heterogeneity, root responses and VI proxies, and an operational remote-sensing pipeline). Part 5 integrates these outputs into a single probabilistic decision-support framework. Because Bayesian Networks are less familiar to many turf research audiences, the Results below retain more methodological context to clarify what the BN is doing, how it is built, and how it is validated on real putting-green data.

1) What the BN-DSS represents and what it was evaluated on

The BN-DSS reconstructs the dissertation's causal logic into an explicit probabilistic framework composed of interacting subgraphs for fertilisation, irrigation, soil moisture, climatic stress, vegetative growth, VI signals, and carbon-cycle related outputs. The system follows the development framework defined in the Methods and extends it by using empirical outputs from Parts 1–4 for calibration and validation.

Implementation and evaluation were performed on a single USGA-specification sand-based putting green (**P14**) instrumented with daily soil sensors (moisture, temperature, salinity) and a local weather station. Management logs from **2022–2024** provided complete records of nitrogen inputs, irrigation volumes, clipping yield, and surface conditioning, forming the empirical basis for BN updating and assessment. Model initialization used the **2022–2023 seasons**, and all performance reported here refers to an independent **93-day** validation window (**31 May to 1 September 2024**).

Three evaluation targets were selected because they cover canopy state, growth response, and irrigation efficiency, which are central to resource-efficient turf management:

1. **NDVI state classification** (low/medium/high relative to hyperspectral reference),
2. Daily clipping volume MAE,
3. Irrigation-related WUE.

2) Step 1. Knowledge extraction from publications (NLP → knowledge graph → BN priors)

Corpus and annotation. A corpus of **136 peer-reviewed papers (2000–2023)** on turfgrass water and nutrient management was harvested. From these, "Results" sections were filtered to **1,712 sentences** annotated with **11 agronomic relation types**. Inter-annotator agreement was substantial (**overall $\kappa = 0.74$**), with relation-level κ ranging approximately **0.68–0.78** and corresponding F1 values **~0.76–0.85** across labels (Table 39; Figure 83).

Table 22. Inter-annotator agreement for eleven agronomic relation types extracted from scientific publications.

Relation	Agreement Metrics		
	Kappa	F1	N of positives
relates_to_biomass	0.74	0.81	284
relates_to_eto	0.71	0.79	60
improves_soil	0.77	0.83	35
relates_to_n_rate	0.69	0.77	170
affects_quality	0.72	0.80	450
correlates_with_gp	0.75	0.82	98
improves_nutrient_effciency	0.73	0.80	170
water_use	0.78	0.85	150
enhances_root	0.7	0.78	90
relates_to_vi	0.68	0.76	92
increases_vigor	0.72	0.80	113

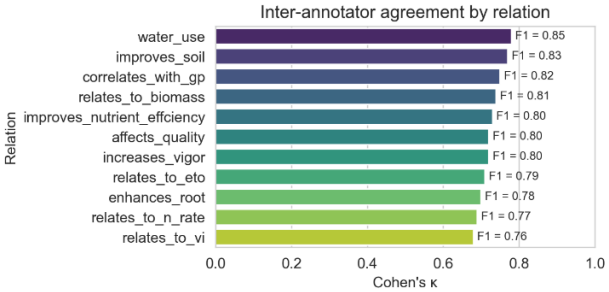

Figure 63. Inter-annotator agreement by relation (Cohens 'k' and F1)results_5

Label distribution and model comparison. The label frequencies are shown in Figure 84. Model evaluation compared BERT, SciBERT, and GPT-4 for relation extraction. GPT-4 achieved the highest overall performance (**Precision 0.81, Recall 0.74, F1 0.77, AP 0.79**), outperforming SciBERT and BERT (Table 40), with precision–recall curves showing GPT-4 maintaining higher precision up to ~0.60 recall before degrading (Figures 85–86).

Table 23. Model comparison metrics

Model	Comparison metrics			
	Precision	Recall	F1	AP
BERT	0.65	0.66	0.66	0.67
SciBERT	0.77	0.69	0.72	0.73
GPT-4	0.81	0.74	0.77	0.79

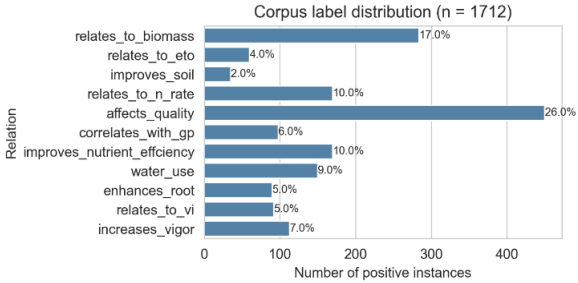

Figure 64. Label distribution for the annotated relation corpus. Frequency distribution of relation labels across the 1,712 annotated sentences used for training and evaluating the NLP extraction pipeline

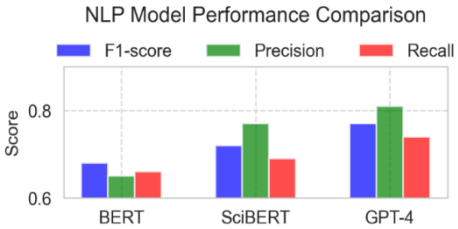

Figure 65. Model performance comparison (BERT, SciBERT, GPT-4) for agronomic relation extraction. Precision, recall, F1, and average precision (AP) metrics demonstrating superior performance of GPT-4 for extracting agronomically meaningful relations, justifying its selection for BN knowledge graph construction

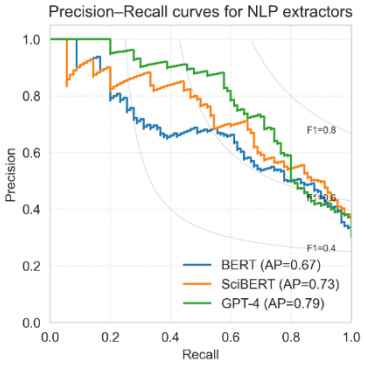

Figure 66. Precision–recall curves for BERT, SciBERT, and GPT-4. Curves illustrating model trade-offs across recall levels. GPT-4 maintains the highest precision for moderate recall values before degrading, making it the most reliable option for high-confidence relation extraction.

Error sources and knowledge graph output. Manual inspection of 300 random false positives/negatives identified two dominant sources: polysemous terms such as "stress" used in both abiotic and biotic contexts (**41% of errors**), and nested relations spanning multiple clauses (**>27%**). Step 1 produced a compact knowledge graph of **32 high-confidence triples**, covering the key interactions needed for the initial DSS state. This knowledge graph seeded the BN structure and supplied prior distributions that were later updated with site-specific data.

3) Step 2. Building and validating the BN (DAG + CPTs + calibration)

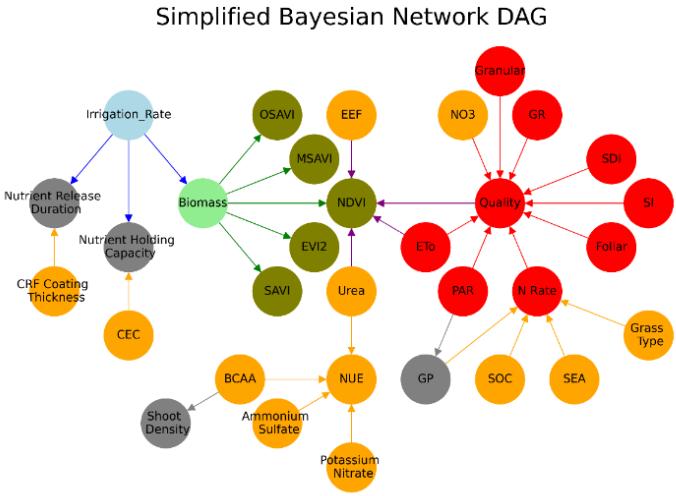

Figure 67. Simplified BN DAG extracted from literature

Structure (DAG). Using the knowledge graph output, the BN was designed to capture the causal chain from climatic drivers → management actions → physiological responses → observed performance metrics. The final DAG (Figure 87) contains **32 nodes**, representing interacting processes relevant to nitrogen management, irrigation, canopy state, and observed outcomes.

CPT initialization and updating. Conditional probability tables (CPTs) were initialized from literature-derived frequency counts and updated using Bayesian estimation with Dirichlet priors ($\alpha_0 = 1.0$). A conditional probability check example for NDVI, Irrigation Rate, and N Rate is shown in Figure 88 to demonstrate how priors interact with empirical evidence within a triad of management–canopy relationships.

Predictive performance (93-day hold-out). On the independent 93-day evaluation period, the BN achieved:

- **NDVI:** accuracy **0.830**, balanced accuracy **0.710** (n = 93)
- **Irrigation_Rate:** accuracy **0.865**, balanced accuracy **0.833** (n = 93)

- **N_Rate:** accuracy **0.873**, balanced accuracy **0.860** (n = 93) (Table 41). A walk-forward test with 14-day warm-up delivered the same NDVI-state classification on each evaluation day (accuracy 0.830; balanced accuracy 0.710). A blocked split (June–July train, August test) reduced NDVI accuracy to **0.74 (not shown)**, supporting the claim that high performance is not due to target leakage. The overall ranking and class-balance-aware performance are summarised in Figure 89, while class-level errors are shown via confusion matrices in Table 42.

Table 24. Predictive performance of the BN on the 93 days evaluation window (31 May – 1 Sep 2024). Confidence intervals calculated with Wilson method (n = 93).

Target	Performance metrics		
	accuracy	balanced_accuracy	n_samples
NDVI	0.830	0.710	93
Irrigation_Rate	0.865	0.833	93
N Rate	0.873	0.860	93

Table 25. Confusion matrices for BN model predictions of (a) Irrigation Rate, (b) NDVI, and (c) Nitrogen Rate on the validation set. Each matrix shows the number of observations in each true–predicted class combination, illustrating classification performance across the three-class targets.

True class	Predicted class								
	Irrigation_Rate			NDVI			N_Rate		
	0	1	2	0	1	2	0	1	2
true_0	48	2	1	48	3	0	24	0	6
true_1	1	17	2	0	23	5	6	20	0
true_2	4	1	24	3	4	4	0	0	37

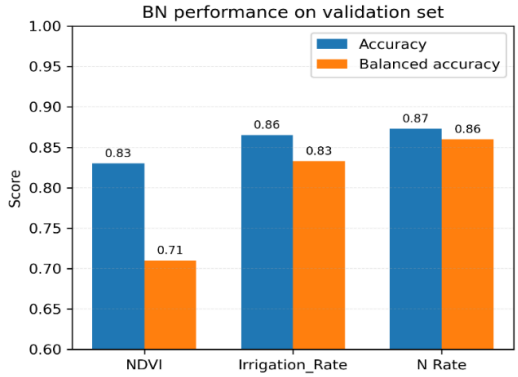

Figure 68. Grouped bar chart showing accuracy (blue) and balanced accuracy (orange) for BN predictions of Irrigation Rate, NDVI, and Nitrogen Rate. Balanced accuracy accounts for class imbalance by averaging recall across classes

Calibration (probabilistic trust). Reliability diagrams were generated for NDVI, Irrigation_Rate_state, and N_Rate_state using equal-frequency binning (minimum 20 samples per bin; merged sparse bins). Calibration was quantified via Expected Calibration Error (ECE). NDVI showed excellent calibration (**ECE = 0.002**), while Irrigation Rate (**ECE = 0.112**) and N Rate (**ECE = 0.084**) showed mild miscalibration, primarily under-confidence at mid-range probabilities (Figure 90).

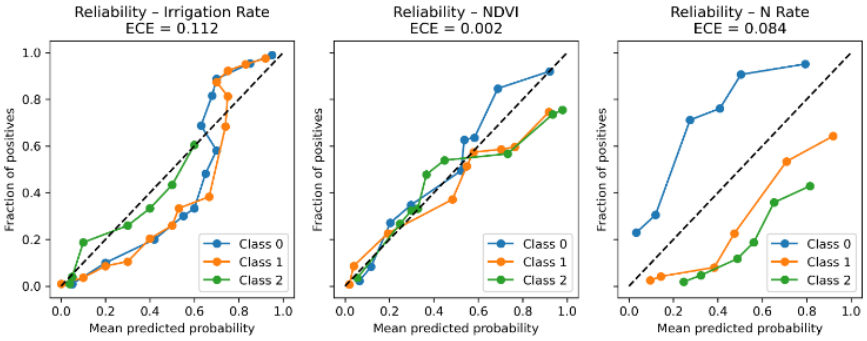

Figure 69. Multi-class reliability diagrams for (a) Irrigation Rate, (b) NDVI, and (c) Nitrogen Rate. Curves plot observed class frequency vs mean predicted probability; the diagonal denotes perfect calibration. ECE (lower is better) is reported per target. Equal-frequency binning (deciles) with ≥20 samples per bin; sparse neighboring bins merged.

4) Step 3. Hybrid integration of data-driven models (site updating without double counting)

Daily evidence pipeline. Daily sensor and weather records from **1 Jan to 31 Aug 2024 (n = 244)** were reserved for dynamic updating of the BN. For focal edges (Irrigation_Rate → Biomass → NDVI; N_Rate → Quality → NDVI), gradient-boosted logistic calibrators (XGBoost; max_depth = 3; n_estimators = 150) estimated edge-specific likelihood ratios that adjust CPT rows, followed by renormalization.

Double-counting safeguard. Predictors already represented elsewhere in the BN (example: Penman–Monteith ET_0) were excluded from calibrator feature sets to prevent reusing the same evidence twice. This is important because redundant evidence can artificially inflate posterior confidence and degrade interpretability.

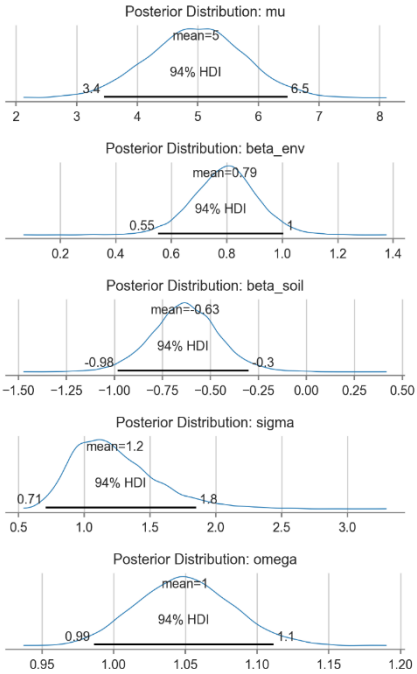

Figure 70. Bayesian model diagnostics. Posterior distributions of key parameters with means and 94% HDIs.

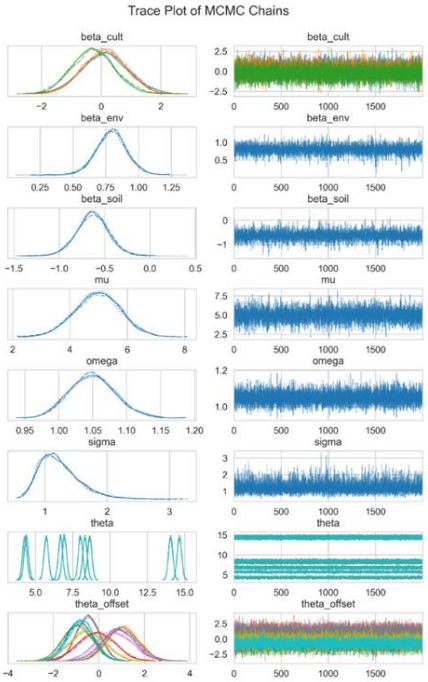

Figure 71. Bayesian model diagnostics. Trace plots for all parameters showing well-mixed Markov chains, indicating good convergence and accurately represented the posterior distribution

Bayesian estimation and diagnostics. Posterior parameters were sampled using NUTS Hamiltonian Monte Carlo (PyMC 5.13; 4 chains; 2,000 iterations; 1,000 warm-up). Posterior distributions were unimodal and approximately symmetric (Figure 91), trace plots showed well-mixed chains (Figure 92), and Gelman–Rubin values were **≤ 1.01** for all monitored parameters (Figure 93), indicating satisfactory convergence.

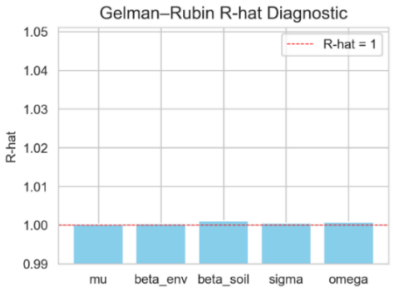

Figure 72. Gelman–Rubin $\hat{R}$ values (all ≤ 1.01)

Posterior predictive checks. Posterior predictive overlays (Figure 94) show close alignment between simulated and observed NDVI states (Bhattacharyya distance **0.06**). Continuous metrics (clipping volume and daily water use) fell within the 95% posterior predictive interval on **89%** and **92%** of days, respectively. These checks indicate that the hybrid updates correct small biases noted in earlier BN outputs without sacrificing calibration.

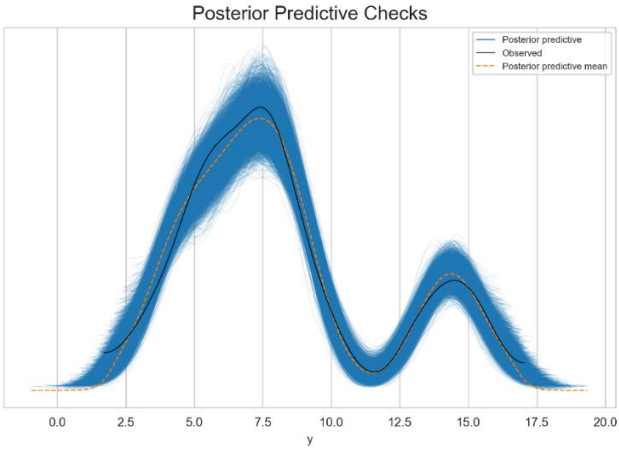

Figure 73. Posterior predictive checks for the Bayesian model. Thin blue curves are draws from the posterior predictive distribution ($\tilde{y}$); the orange dashed line is the posterior-predictive mean; the solid black line is the observed response. The observed series lies largely within the envelope of simulated curves, indicating that the model reproduces the main structure and variability of the data.

5) Decision impact analysis (counterfactual scenarios)

Using updated network posterior means, outcomes were simulated for three management scenarios over the evaluation period: baseline (as managed), **−25% nitrogen**, and **ET-optimized 80% irrigation**. Relative to baseline, the ET-optimized irrigation scenario maintained nearly the same probability of high NDVI while improving irrigation WUE, whereas uniform N reduction reduced clipping production and lowered NDVI probability. Specifically (Table 43):

- **Baseline:** Mean NDVI_state=High **0.86**; Clip-volume **9.58 ml m^{-2} d^{-1}**; Irrigation WUE **1.53 g biomass L^{-1}**
- Reduced N (−25%): NDVI_high 0.78 (−10.3%); Clip-volume 8.19 (−16.3%); WUE 1.35 (−16.3%)
- ET-optimized irrigation (80%): NDVI_high 0.84 (−2.4%); Clip-volume 8.95 (−6.4%); WUE 1.65 (+14.9%)

In an additional counterfactual statement, switching from low to high daily N application increased the probability of NDVI=High by **0.18 ± 0.05 (p < 0.01)**, while incurring a **12% risk of over-fertilization**.

Table 26. Decision impact analysis (Bayesian network counterfactuals

Scenario	Impact metrics		
	Mean NDVI_state = High	**Mean Clip-volume (ml m^{-2} d^{-1})**	**Mean Irrigation WUE (g biomass L^{-1})**
Baseline (as managed)	0.86	9.58	1.53
Reduced N (-25 %)	0.78 (-10.3 %)	8.19 (-16.3 %)	1.35 (-16.3 %)
ET-optimized irrigation (80%)	0.84 (-2.4 %)	8.95 (-6.4 %)	1.65 (+14.9 %)

Part 5 demonstrates that the dissertation's separate analytical components can be reconstructed into a probabilistic system that (i) predicts key turf states with good accuracy and interpretable uncertainty, (ii) remains calibratable as new site data arrive, and (iii) supports explicit counterfactual comparisons of management strategies. This provides the necessary bridge to the Conclusions and Contributions, where the work is positioned as both a scientific framework and an operational pathway toward more resource-efficient, carbon-aware management of sand-based putting greens.

4 Conclusion

This dissertation integrated four management levers, nitrogen supply, irrigation strategy, root system development, and canopy condition, into a unified understanding of soil carbon sequestration on intensively managed sand-based putting greens. Across experiments, modelling, and remote-sensing analyses, the evidence converged on the following conclusions:

1. Soil-carbon outcomes are governed by coupled inputs and losses rather than any single variable. Carbon inputs are primarily driven by clipping production and root turnover, while carbon losses increase under moisture-driven mineralisation and thatch decomposition, and when stress suppresses physiological carbon gain.

2. Sand-based putting greens can approach carbon-neutral or mildly carbon-positive behaviour within a favourable operating range. In the studied sand profiles, this regime was characterised by moderate nitrogen inputs, deficit-oriented irrigation maintaining a stable moisture band (notably around 18–26% VWC), deeper and seasonally stable rooting, and positive or neutral VI trajectories consistent with sustained growth without prolonged stress.

3. Failure modes shift the system toward net carbon loss and explain slow but directional SOM change. Persistent wet pockets, chronic nitrogen oversupply, shallow rooting, and repeated high-temperature stress increased the likelihood of net carbon loss. Multi-year SOM trajectories respond slowly but directionally because they integrate the accumulated effects of management on productivity, decomposition dynamics, and belowground allocation across seasons.

4. Nitrogen dynamics are stress-modulated and link short-term performance signals to long-term SOM trends. Short stress windows constrain growth and uptake, shaping both manager-applied nitrogen patterns and cumulative nitrogen removal. Over multiple years, sustained nitrogen regimes are reflected in SOM trajectories, positioning SOM as a slow-cycle sustainability constraint.

5. Irrigation determines depletion–recovery dynamics on sand greens, and spatial heterogeneity makes averages insufficient. ETc-driven depletion and moisture inertia control day-to-day VWC behaviour, but within-green non-uniformity explains why local stress or saturation can occur even when mean VWC appears acceptable. Spatial diagnostics therefore materially improve interpretation of moisture-related risk.

6. Root condition is a stabilising mediator connecting water and nitrogen efficiency to belowground carbon allocation. Deficit-oriented irrigation consistently supported deeper and more persistent roots during heat-stress windows, and root length provides a practical medium-term constraint for interpreting resilience, uptake capacity, and carbon-allocation potential.

7. Remote sensing provides scalable canopy-state evidence when AOIs are standardised and VI space is reduced. U-Net segmentation enables turf-only AOI masking that protects VI validity, while VI-family reduction supports interpretable canopy indicators that can complement in-situ measurements for stress and performance monitoring.

8. A Bayesian DSS can operationalise the causal structure and remain adaptable as new evidence arrives. The BN framework integrates literature-derived priors with site-specific sensor and VI evidence, supports probabilistic state inference with calibration diagnostics, and enables scenario testing under uncertainty. Across sites, thresholds may shift, but the hierarchy of controls linking moisture, nitrogen, stress exposure, and belowground resilience remains stable.

5 Contributions

5.1 Scientific contributions

1) Carbon-aware operating-envelope framework for sand-based putting greens

This dissertation introduces a carbon-aware "narrow operating envelope" framework for intensively managed sand-based putting greens, formalising how nitrogen supply, moisture regime, stress exposure, rooting behaviour, and canopy dynamics jointly constrain net soil-carbon outcomes in rapid-turnover sand profiles. The framework links four controllable levers (N, irrigation, roots, canopy state) to two carbon pathways: carbon inputs governed by clipping production and root turnover, and carbon losses governed by moisture-driven mineralisation, thatch decomposition, and stress-mediated constraints on physiological carbon gain. By expressing these relationships as a mechanistic hierarchy, the work provides a structured basis for interpreting why similar turf quality can correspond to different long-term carbon trajectories under different management histories.

2) Explainable temporal irrigation dynamics with actionable VWC and ETc thresholds

The irrigation analysis quantifies sand-profile moisture behaviour as a narrow working band with a drainage-driven upper plateau and increased instability under depletion. SHAP interpretation confirms a physically coherent driver hierarchy where current VWC and ETc dominate next-day moisture dynamics and identifies threshold-like behaviour in both VWC and ETc. These results support discretisation into interpretable moisture and evaporative-demand states suitable for decision modelling and transfer across greens with similar sand-rootzone hydraulics.

3) Spatial irrigation heterogeneity as a within-green diagnostic layer

The dissertation demonstrates that within-green spatial heterogeneity materially shapes realised stress exposure and cannot be inferred reliably from mean VWC alone. DU, CV, moisture-class area fractions, and time-series clustering reveal persistent dry and wet zones

and quantify their seasonal stability. This provides a scientific basis for separating temporal depletion–recovery dynamics from spatial distribution effects and for diagnosing when patchiness is driven by hydraulics, micro-topography, or surface-condition constraints rather than scheduling alone.

4) Root system development as a mechanistic mediator between management and belowground allocation

The root module establishes predictable seasonal rooting trajectories and stable treatment hierarchies under contrasting irrigation regimes, with deficit-oriented irrigation supporting deeper and more persistent roots during heat-wave windows. Predictive modelling shows that environmental water-balance drivers explain a substantial share of root-length variability, while lag-aligned canopy spectral signals provide secondary, physiologically coherent proxy information. Root condition is thereby positioned as a medium-term constraint linking irrigation regime and nutrient dynamics to belowground allocation processes relevant to carbon persistence.

5) Defensible remote-sensing pipeline for turf-only AOIs and interpretable VI compression

A high-accuracy U-Net semantic segmentation front end standardises turf-only AOIs and removes non-turf contamination from VI time series, enabling consistent multi-year monitoring on heterogeneous golf-course imagery. Multi-season clustering compresses large VI archives into repeatable canopy regimes, and similarity-family analysis establishes stable functional VI families (structural NIR-based, colour-stress, soil-adjusted, red-edge, and non-linear/saturated). Together, these components provide a principled, physiologically interpretable dimensionality-reduction strategy that supports robust canopy-state inference across surfaces and sites.

6) Probabilistic integration and validation of a Bayesian Network DSS

The dissertation establishes a reproducible knowledge-to-model pathway in which literature-derived priors are extracted via NLP, encoded as BN structure and CPT priors, and updated with site-specific evidence. The BN is validated on independent putting-green data using accuracy and class-balance-aware metrics, while calibration diagnostics quantify probabilistic trust. The framework enables counterfactual scenario testing and makes trade-offs explicit under uncertainty, providing an integrating layer that links moisture, nitrogen, canopy state, and root-related constraints into a single decision object.

5.2 Scientifically applied contributions

1) Carbon-aware operational decision logic for sand-based greens

The operating-envelope framework is translated into a practical decision logic and diagnostic checklist for daily to weekly management: avoid chronic wetness and chronic nitrogen oversupply that accelerate decomposition and losses; avoid chronic deficiency that collapses

growth and root turnover; manage short stress waves proactively; and protect rooting depth as a resilience and carbon-allocation safeguard. This applied framing supports field diagnosis of whether carbon risk is dominated by wetness, oversupply, deficiency, or repeated stress exposure, rather than treating turf performance as a sufficient proxy for sustainability.

2) Irrigation scheduling rule-set from VWC and ETc state thresholds

The dissertation delivers a field-usable threshold system for sand greens: maintain VWC in a stable 18–26% band, treat ~16–18% as a depletion-prone "start irrigation" boundary, and treat ~28–30% as a drainage/non-beneficial ceiling to avoid wasted irrigation and potential leaching below sensor depth. ETc state classes (<2, 3–5, >5.5 mm day^{-1}) support risk-aware timing by anticipating rapid drying under high evaporative demand, enabling scheduling decisions that balance stress avoidance with resource efficiency.

3) Spatial remediation workflow for patchy moisture

Spatial diagnostics enable applied separation of scheduling problems from distribution problems. DU/CV trends, moisture-class area fractions, and persistent zone identity support targeted interventions (nozzle tuning, local drainage correction, aeration, wetting agents) without destabilising whole-green schedules based on misleading averages. This within-green layer provides a practical pathway to reduce localised stress and saturation risk while improving confidence in irrigation decisions.

4) Root-risk forecasting to refine irrigation thresholds and nitrogen safety margins

Seasonal rooting envelopes and regime-specific predictors support identification of shallow-root risk windows, especially during heat-wave periods. Root condition can refine irrigation thresholds and timing and inform nitrogen safety posture by reflecting uptake capacity, leaching vulnerability, and resilience risk under repeated stress. This enables managers to adjust water and nitrogen decisions proactively based on belowground capacity rather than reacting only to aboveground symptoms.

5) Implementable VI evidence nodes for routine monitoring and DSS integration

A compact, interpretable set of VI-family representatives is proposed for DSS evidence: a structural index (NDVI or GNDVI), a colour-stress index (MGVRI or VARI), a soil-adjusted index (MSAVI), and optionally a red-edge index (NDRE) where biochemical gradients are informative. Combined with turf-only AOI masks, these indices enable scalable time-series monitoring and within-green heatmaps aligned to stress and performance interpretation, supporting consistent evidence streams for nitrogen, irrigation, and root modules.

6) BN-enabled decision support with uncertainty and counterfactual evaluation

The BN-DSS converts empirical findings into operational probabilistic reasoning: it updates site states from sensor and VI evidence, propagates uncertainty across linked processes, and supports counterfactual scenario evaluation. This enables quantified comparisons of irrigation

and fertilisation strategies, reducing reliance on static schedules or single-variable heuristics and improving transparency of decision rationale

5.3 Practically applied scientific contribution

Operational SMART dashboard implementation

A functional, modular dashboard was developed as the user-facing implementation layer of the SMART BN-DSS, translating the dissertation's thresholds and state definitions into day-to-week operational decisions. The dashboard consolidates weather and sensor evidence, computes shared derived drivers used across modules (GP, ET/ETc, stress indicators), and presents aligned state interpretations across irrigation, fertilisation, root development, canopy monitoring, and organic-matter tracking. This demonstrates that the dissertation's framework is deployable in a reproducible workflow that mirrors the BN subgraphs and their dependencies.

As a practical decision-support tool, the dashboard enables site-specific historical diagnosis, short-horizon planning, and scenario exploration while maintaining an auditable record of actions and outcomes. By integrating temporal rules (threshold-based scheduling), spatial diagnostics (zone-aware moisture interpretation), and remote-sensing evidence (AOI-based VI trajectories and heatmaps), it provides a coherent interface for adaptive management under uncertainty and supports carbon-aware optimisation within routine maintenance constraints